Title: Functional morphology of the hindlimb during the transition from sprawling to parasagittal gaits in synapsid evolution

Author: Mark A. Wright[1, 2]

Supervisors: Prof. Dr. Stephanie E. Pierce[1], Prof. Dr. R.S. Rampal Etienne[2]

Affiliation: [1]Museum of Comparative Zoology, Harvard University, 26 Oxford Street, Cambridge, MA, United States; [2]Groningen Institute for Evolutionary Life Sciences, University of Groningen, 9700 CC Groningen, Netherlands

Correspondence: markwright@fas.harvard.edu

Running page heading: Hindlimb Function Transition Synapsids

Abstract

Mammals are characterized by rich diversity in hindlimb morphology, locomotory specialization, and ecological habit. As mammalian species spread throughout the globe occupying novel environments, some modified their hindlimbs to reflect the challenges of these new environments. However, it is unclear whether disparate limb morphology was the driver or the result of this ecological diversification. Exploring the relationship between ecology and morphology during the transition from the earliest synapsids (mammalian ancestors) to basal mammals requires a comparative framework connecting morphology to locomotory function. This transition included a postural shift in hindlimb orientation. The earliest synapsids had limbs abducted to their sides that operated with the same sprawling movement common in many extant lizards and salamanders. However, the first mammals had limbs rotated underneath the body, upright, that operated primarily in a parasagittal plane of movement. Here, two species (the extinct sphenacodontid, *Dimetrodon milleri*, and the extant opossum, *Monodelphis domestica*) are used to represent an early and late character state, respectively, of hindlimb function during this transition. The opossum was stained using phosphomolybdic acid (PMA) for soft tissue contrast, and both specimens were scanned using microcomputed tomography (μCT). With three-dimensional modeling software, musculoskeletal models were created for each specimen to interpret functional morphology of the hindlimb at two stages during this evolutionary transition. The results here show that basal synapsids had increased mechanical advantage during sprawling movements (higher abduction-adduction moment arms) while the proximal hindlimb of ancestral therian mammals functioned as joint-stabilizers during parasagittal stances (negative sloping flexion-extension moment arms that cross through zero). Sensitivity analyses of two model-building parameters (neutral pose orientation and muscle attachment site) confirm that differences in functional interpretations are not caused by limitations during model construction.

Introduction

Synapsida, a group that includes mammals and all extinct vertebrates more closely related to mammals than any other extant species, is a morphologically and ecologically diverse clade. While non-mammalian synapsids are composed primarily of terrestrial quadrupeds with limited ecological scope, mammals occupy habits around the world, ranging in environment and in locomotory specialization. These specializations include cursorial, saltatorial, scansorial, fossorial, natatorial, graviportal, and bipedal locomotion as well as generalized or ambulatory mammals that are not specialized for one particular mode of locomotion (Polly, 2007). In some cases, locomotory specialization has been linked to diversity in limb morphology. For example, beavers and water opossums have hind feet that are webbed, providing a large surface area for propelling through water (Osburn, 1903). Antelopes have long, slender legs and two-toed feet that allow early predator detection in African savannahs followed by quick escape (Maynard Smith and Savage, 1956; Polly, 2007). The limited ecomorphological scope of basal synapsids suggests that increased diversity in hindlimb morphology may have allowed the ancestors of mammals to inhabit different environments around the world. Despite a copious fossil record (Kemp, 1978; Hopson, 1987; Benson, 2012), the tempo and mode of phenotypic evolution remains untested within this clade. An understanding of functional hindlimb morphology across synapsids is necessary to establish a comparative framework for investigating the relationship between ecological diversification and expansion of locomotory capability during this transition.

From basal synapsids to the ancestors of therian mammals, the hindlimb underwent a postural shift with novel functional consequences (Polly, 2007). “Pelycosaurs”, the earliest synapsids that appeared during the Carboniferous (>310 mya), had large pelvic girdles with short, heavy hindlimbs abducted to their sides. They likely moved with the same sprawling gait common in extant lizards and salamanders (Kemp 1980; Blob 2001; Kemp 2005; Kemp 2006). One “pelycosaur” lineage gave rise to therapsids (Benson, 2012), which were abundant during the Permian (~250-300 mya). Musculoskeletal reconstructions of ancestral therapsids suggest both sprawling and parasagittal gaits were possible (Blob, 2001; Kemp, 2006), and later non-mammalian cynodonts share this dual-gait functionality (Kemp, 1980). The ability to alternate between two step cycles is also found in

extant quadrupeds such as the crocodile, which can switch between an erect high walk and a lizard-like sprawling gait (Brinkman, 1980). In contrast, the first therian mammals, arising from a cynodont lineage by the end of the Triassic (>200 mya) (Meredith *et al.*, 2011; O'Leary *et al.*, 2013; Springer *et al.*, 2013), had hindlimbs that were more adducted underneath the body and acted primarily along a parasagittal plane of movement (Jenkins 1971; Kemp 1978; Polly 2007). The same postural transition from sprawling to upright hindlimbs has occurred independently in other terrestrial groups including Dicynodontia during the Middle Triassic (Fröbisch, 2006). The lineage leading to the dicynodont *Tetragonias njalilus* evolved several morphological characters such as a medially-projecting femoral head, a prominent lateral trochanter of the femur, and an anterior elongation of the ilium that each contribute towards more efficient locomotion in a parasagittal plane of movement (Fröbisch, 2006). While the adaptive potential of both sprawling (Rewcastle, 1983) and parasagittal (Sargis, 2002) gaits has been described, modern biomechanical methods for reconstructing hindlimb function in fossils have not been applied to test functional hypotheses about locomotory capability of synapsids during this transition.

This study uses three-dimensional musculoskeletal modeling techniques to characterize the functional morphology of the hindlimb in early synapsids and the ancestors of therian mammals. Musculoskeletal models are created for the extinct "pelycosaur", *Dimetrodon milleri*, and the extant marsupial, *Monodelphis domestica*, to represent the basal synapsid and the ancestral mammalian condition, respectively (Figure 1). *D. milleri* was an abundant synapsid that existed prior to this postural transition, while *M. domestica* has often been used as a modern analogue for plesiomorphic mammalian anatomy (Argot, 2001; Ferner, Zeller and Renfree, 2009). Previous studies have used musculoskeletal models to quantify the relationship between moment arms and joint angles for muscles of interest in the mouse (Charles, Cappellari, Spence, Hutchinson, *et al.*, 2016; Charles, Cappellari, Spence, Wells, *et al.*, 2016), rat (Johnson *et al.*, 2008), hare (Williams, Payne and Wilson, 2007), feline (Burkholder and Nichols, 2004), and gorilla (Goh *et al.*, 2017). The moment arm of a muscle is the perpendicular distance between the joint axis of rotation and the line of action of the muscle (Payne *et al.*, 2006; Brassey, Maidment and Barrett, 2017). It represents the leverage, or the load applied to the joint axis when the muscle exerts a force, and is a proxy for mechanical advantage. A muscle with a larger moment arm more

effectively uses its contractile force to produce a rotational force around a joint and subsequently reduces overall organism energy expenditure during movement. Moment arms have been used to interpret locomotory function in extinct taxa (Hutchinson *et al.*, 2005; Bates and Falkingham, 2012; Maidment, Bates and Barrett, 2014) through careful validation of reconstruction techniques with relevant extant data (Brassey, Maidment and Barrett, 2017). Sensitivity analyses are useful for validating methods of interpretation in extinct forms by examining the consequences of error in model parameter estimates (Hutchinson, 2004a, 2004b; Brassey, Maidment and Barrett, 2017). Moment arm analysis allows for quantitative species-level comparisons of functional morphology and can be estimated in extinct species using validated reconstruction techniques.

In this study, musculoskeletal models are created using microcomputed tomography (μCT) scans of the hindlimbs of *D. milleri* and *M. domestica* to test functional hypotheses about the sprawling and parasagittal gaits, respectively, of basal synapsids and the ancestor to therian mammals. Interactive motion modelling software is used to generate moment arms about each rotational axis of the hip joint for proximal hindlimb muscles in both specimens. These moment arms are contrasted between homologous muscles in *D. milleri* and *M. domestica* to compare energetically efficient movements in basal synapsids and the ancestor to therian mammals. Both musculoskeletal models are validated through sensitivity analyses of modeling parameters. This study provides the starting framework for large-scale comparisons of locomotory capability and ecological diversification to investigate the rate and drivers of phenotypic evolution in synapsids.

Materials and Methods

Specimen Preparation

Four *Dimetrodon milleri* left hindlimb bones (pelvis, femur, tibia, and fibula; specimen: MCZ 1365) were selected from the Vertebrate Paleontology collections at the Museum of Comparative Zoology at Harvard University (Figure 2; Table 1) and scanned using a HMXST225 microcomputed tomography (μCT) unit at 130 kV and 165 μA with a 0.5 mm copper filter. For *Monodelphis domestica*, a fresh, cadaveric specimen was

immersed in 2.5% solution of phosphomolybdic acid (PMA) to enhance soft tissue contrast (Pauwels *et al.*, 2013) (Figure 3; Table 1). The specimen was scanned using a Skyscan 1173 μCT unit at 139 kV and 71 μA with a 1.0 mm aluminum filter at 3 weeks, 5 weeks, and 8 weeks following PMA immersion to ensure full penetration of muscle tissue. The resulting tomograms for the *D. milleri* scans and the 8-week *M. domestica* scan were reconstructed as a TIFF image stack using CT Pro 3D software (Nikon Metrology Inc., Brighton, MI, USA) and imported into Mimics v19 (Materialise, Leuven, Belgium) for segmentation. Each individual bone in both specimens and each muscle in *M. domestica* were segmented as individual objects. For *M. domestica*, the left hindlimb was used to be consistent with the *D. milleri* specimen. All bone and muscle objects for both specimens were exported as binary STL files and smoothed using quality control features available in Mimics, MeshLab, and Autodesk Meshmixer.

Inferring Musculature in Dimetrodon

While staining allows soft tissue structures to be modeled directly (see Figure 4 for *M. domestica* hindlimb musculature and Table 2 for muscle abbreviations), muscles in extinct species must be inferred using the extant phylogenetic bracket (EPB) method (Witmer, 1995). This method works by investigating the soft tissue anatomy of at least two outgroup species closely related to the fossil species. The first should be an extant sister group to the fossil species, and the second should be an extant sister group to the clade formed by the first two species (Figure 5). Two conditions are evaluated to infer soft tissue anatomy in the fossil species: (1) the presence of homologous soft tissue structures in both extant outgroups mentioned above, and (2) the presence of similar osteological correlates corresponding to these soft tissue structures in both outgroups as well as the fossil species. In this study, the soft tissue structure in consideration is always the muscular attachment site. The osteological correlate can be any readily identifiable bony landmark, such as a trochanter, condyle, ridge along the bone, or, preferably, muscle scars (Polly *et al.*, 2016; Brassey, Maidment and Barrett, 2017).

Inferring soft tissue anatomy in the fossil species is relegated a confidence level depending on how well it meets the specified conditions. Level I Inference is the highest degree of confidence and indicates that both

conditions are met (i.e. the homologous soft tissue structure is present in both extant outgroups and the same osteological correlate is present in both outgroups as well as the fossil species). Level II Inference occurs when either outgroup has an identical osteological correlate to the fossil species, but the other outgroup species lacks this bony landmark. In this case, the most parsimonious inference is that the soft tissue structure is homologous to the one present in the outgroup species with the same osteological correlate. Level III Inference occurs when no outgroup species have osteological correlates identifiable in the fossil species and indicates the lowest degree of confidence in the soft tissue inference. The phylogenetic bracket used to infer muscular attachments for *D. milleri* is illustrated in Figure 6. For *D. milleri*, the 26 muscular attachments of the 13 proximal hindlimb muscles inferred using this method include 16 Level I Inferences, 10 Level II Inferences, and no Level III Inferences (Tables 3 and 4; Figure 7) (Romer, 1922; Jones, 1979; Diogo *et al.*, 2016). *Diogo 2018* often describes general areas for muscular attachments rather than the specific bony features that are needed for inference using the EPB method. For Marsupialia in the EPB, the muscular geometry of *M. domestica* from this study was also considered when comparing osteological correlates (Figure 4; Table 2).

Musculoskeletal Model Construction

The smoothed STLs for all hindlimb bones of *D. milleri* and all hindlimb bones and muscles of *M. domestica* were imported to separate workspaces in 3D Studio Max (3DSM) software (Autodesk, San Rafael, CA, USA). Coordinate systems for each specimen were set up following previously established methods (Hutchinson *et al.*, 2005, 2015). Three segments were created for each species model (pelvis, thigh, and leg) and were composed of the bones present in that region of the hindlimb (Table 5). Axes of rotation were oriented so that the x-axis points cranially, the y-axis points distally, and the z-axis points laterally for each joint. The orientations of these axes were recorded by indicating two points on each line: the center of the joint and a point in space shifted 1 mm along the positive direction of the axis (Table 5). Because the geometric shapes available in 3DSM did not closely match the external anatomy of the acetabulum or proximal femur in *D. milleri*, the origin of the pelvis was determined by averaging the coordinates of three points spaced approximately equidistant along the acetabular

ridge. In *M. domestica*, a spherical primitive fit into the acetabulum, and the center of the primitive was used as the origin of the pelvis. The origin of the thigh in *M. domestica* was similarly found by fitting a spherical primitive to the femoral head and taking the coordinates of the center of the primitive. In constructing a neutral pose for *D. milleri*, the proximal aspect of the femur matched closely the morphology of the acetabular ridges on the pelvis. The neutral position of the femur relative to the pelvis was set as the best fit to this bony ridge. Similarly, the neutral position of the tibia and fibula were determined referencing the external anatomy of the femoral condyles. For *M. domestica*, the neutral pose was set as the position of the bones in the dissected CT scans. To assess the impact of neutral pose orientation on interpreted muscle function, two additional poses were modeled to reflect (1) the method used in *Hutchinson 2015* and *Charles 2016* where all joint angles are set to 0° and (2) the orientation of the hindlimb during mid-stance in *Didelphis virginiana* (Jenkins, 1971). A sensitivity analysis was conducted to compare muscle moment arms in each of these three neutral poses.

Joint spacing in the *D. milleri* model was estimated from three established scaling relationships in the literature (Figure 8): between stylopodial circumference and body mass in quadrupedal terrestrial tetrapods (Campione and Evans, 2012), between body mass and cartilage thickness at the femoral condyles in therian mammals (Malda *et al.*, 2013), and between maximum cartilage thickness at the knee and hip joints in placental mammals (Simon, 1970). Humoral and femoral midshaft circumference were recorded at five locations near the midshaft using the Measure Length tool on smoothed meshes in 3-Matic software (Materialise, Leuven, Belgium). The minimum humoral and minimum femoral midshaft circumference from these five trials were summed and logged to calculate an estimated body mass for *D. milleri* of 27.3 kg. This body mass is smaller than the previous estimate for this specimen (47 kg) based on limb length (Romer and Price, 1940), smaller than estimates of body mass in sphenacodontids (52-83 kg), and much smaller than the largest *Dimetrodon* specimens (~254 kg) (Kemp, 2006). Total joint space at the knee and hip joints (double the articular cartilage) in *D. milleri* were estimated to be 1.8 mm and 1.5 mm, respectively. For this thesis, Romer's estimate of 47 kg was used in construction of the model due to differences in measuring techniques for stylopodial circumference (methods from *Campione 2012* incorporated thin paper measuring tapes of different widths). Because quadrupedal terrestrial tetrapods vary in

body size by a magnitude of five (0.05 kg to 6,435 kg) (Campione and Evans, 2012), the difference between 47 kg and 27.3 kg is negligible for calculating cartilage thickness. Joint spacing was implemented in the model by shifting the distal segment of the joint away from the body in the direction of the long axis of the bone. For *M. domestica*, joint spacing was not adjusted from the dissected position of the stained hindlimb.

After each musculoskeletal model was positioned in a neutral pose, the bones were decoupled from their parents, moved to world origin, and exported as binary STLs. Muscle attachment coordinates were recorded for *D. milleri* by selecting the vertex on the bony mesh in the center of the inferred attachment site (Table 6) and for *M. domestica* be selecting the vertex on the bony mesh closest to the proximal or distal aspects of each individual muscle (Table 7). For five of the muscles in *M. domestica* with broad attachment surfaces (obturator externus, obturator internus, adductor longus, pectineus, and biceps femoris posterior), coordinates were recorded at multiple sites to assess variation in interpreted muscle function with respect to small shifts in muscle attachment site. For each model, joint ranges of motion were determined by rotating the distal segment along each respective axis until it collided with another bony structure (Table 8). This method overestimates the amount of rotation during kinematic movements constrained by collisions with soft tissue structures, though this smaller subset of soft tissue-constrained rotation is guaranteed to be contained within the overestimated range.

Motion Analysis of Musculoskeletal Models

For each model, joint and muscle text files were created for loading the hindlimb into Software for Interactive Musculoskeletal Modeling (SIMM; Musculographics, Santa Rosa, CA, USA) (Figure 9). For each bone in both models, muscle paths were prevented from intersecting bony meshes by adding wrap objects and via points to the SIMM joint file (Figures 10 and 11; Tables 9 and 10). For *M. domestica*, segmented muscles were temporarily added to the SIMM joint file to aid in constraining muscle paths. Muscle moment arms were then plotted as a function of joint angle for each individual muscle of the proximal hindlimb in both *D. milleri* and *M. domestica*. In comparing homologous muscle function between *D. milleri* and *M. domestica*, absolute moment arm values were scaled by femur length following previous moment arm comparative methods (Charles,

Cappellari, Spence, Wells, *et al.*, 2016). For relevant muscles, moment arm values were also compared directly to the kangaroo rat (*Dipodomys deserti*), another mammalian hindlimb with publicly available moment arm data compatible with SIMM.

To assess total joint function, the moment arm values of all muscles that act on the hip were summed about each rotational axis throughout the range of motion of that axis (Hutchinson *et al.*, 2005). This summed relationship shows the optimal joint angle along each rotational axis that maximizes leverage. Comparing these scaled values between *D. milleri* and *M. domestica* shows how total hip joint function changed during the transition from early synapsids to therian mammals.

Results

Muscle moment arms in *D. milleri*

Moment arms were plotted against joint angle for each muscle of the proximal hindlimb that acts on the hip joint in *D. milleri* (Figure 12). The joint angle for each rotational axis represents its range of motion (Table 8). Abduction, internal rotation, and flexion are denoted by positive moment arm values with respect to the neutral pose, while adduction, external rotation, and extension are represented by negative moment arm values. The range of motion was similar for all three axes of rotation in the *D. milleri* hip joint (abduction-adduction: 70°; long axis rotation: 95°; flexion-extension: 85°). Flexor tibialis externus (FTE) had the greatest peak abduction moment arm (50.5 mm at 45°), while pubotibialis (PT) had the greatest peak adduction moment arm (-69.1 mm at -20°). Other muscles with large moment arms about this rotational axis include flexor tibialis internus (FTI) and iliofibularis (IF) as hip abductors and gracilis (GR) and adductor femoris (AF) as hip adductors. Iliotibialis (IT) crossed a moment arm of 0° with a positive slope, meaning that it functions as a hip abductor in abducted poses and a hip adductor in adducted poses.

About the flexion-extension axis, iliotibialis (IT) had the greatest peak flexion moment arm (54.6 mm at 20°), while flexor tibialis internus (FTI) had the greatest peak extension moment arm (57.0 mm at -37°).

Iliofibularis (IF) was the only other muscle with a consistently large flexion moment arm. Flexor tibialis externus (FTE) and gracilis (GR) both also had relatively large extension moment arms. Like the abduction-adduction axis, several muscles crossed a moment arm of 0° with a positive slope. Puboischiofemoralis internus (PIFI), psoas minor (PMI), sartorius (SA), and pubotibialis (PT) all function as hip flexors in flexed poses and hip extensors in extended poses, though none of these muscles have relatively large flexion or extension moment arms.

For long axis rotation, flexor tibialis internus (FTI) had the greatest peak internal rotation moment arm (13.8 mm at -28°), while puboischiofemoralis internus (PIFI) had the greatest peak external rotation moment arm (-20.4 mm at 9°). The only other muscle with a consistently large internal rotation moment arm was flexor tibialis externus (FTE), while psoas minor (PMI) was the only other muscle with a consistently large external rotation moment arm. Unlike the other rotational axes, no muscles crossed a moment arm of 0° with a positive slope. Instead, adductor femoris (AF), ischiotrochantericus (IS), gracilis (GR), and iliofibularis (IF) all crossed a moment arm of 0° with a negative slope. These muscles function as external rotators when the hip is internally rotated and as internal rotators when the hip is externally rotated. Of these muscles, ischiotrochantericus (IS) had the largest shift in function from peak internal rotation moment arm (9.8 mm at -55°) to peak external rotation moment arm (-16.0 mm at 31°).

Muscle moment arms in *M. domestica*

The same method was used to create plots for *M. domestica* with moment arm represented as a function of rotating each muscle through its maximum range of motion (denoted as joint angle) (Figure 13; Table 8). Unlike *D. milleri*, the range of motion about the flexion-extension axis (140º) was considerably larger than the range of motion about the abduction-adduction axis (80°) or the long axis (70°). For this axis, sartorius (SA) had the greatest peak flexion moment arm (11.6 mm at -4°), and no other muscles had relatively large flexion moment arm peaks. For hip extension, gracilis had the greatest peak extension moment arm (10.2 mm at -2°). Several other muscles also had large extension moment arm peaks, including adductor magnus (AM), semimembranosus (SM), and semitendinosus (ST). No muscles crossed a moment arm of 0° with a positive slope, but pectineus

(PEC), obturator externus (OE), gemellus (GE), rectus femoris (RF), sartorius (SA), adductor brevis (AB), and adductor longus (AL) each crossed 0° with a negative slope, indicating that they are particularly effective at pulling the femur back towards its neutral pose but not at pushing it away in either direction.

Hip abduction, like hip extension, had several muscles with large abduction moment arms. Of these muscles, semitendinosus (ST) had the greatest peak abduction moment arm (4.2 mm at 75°) with biceps femoris posterior close behind (4.1 mm at 74°). Semimembranosus (SM) also had a consistently large abduction moment arm at all joint angles. Adductor longus (AL) had the greatest peak adduction moment arm (6.6 mm at 25°), while sartorius (SA) and adductor brevis (AB) also had consistently large adduction moment arms across all joint angles. Gluteus maximus (GM), adductor magnus (AM), and gracilis (GR) were the only muscles to cross a moment arm of 0°, each with a positive slope. Gluteus maximus had the largest shift in function of these muscles from peak adduction moment arm (1.1 mm at -5°) to peak abduction moment arm (1.3 mm at 75°).

For long axis rotation, gluteus maximus (GM) had the greatest peak internal rotation moment arm (3.5 mm at 20°), while pectineus (PEC) had the greatest peak external rotation moment arm (3.2 mm at 18°). While gluteus maximus had its peak internal rotation arm at internally rotated joint angles, several muscles had large peak internal rotation moment arms at externally rotated joint angles. These muscles include semitendinosus (ST), semimembranosus (SM), gracilis (GR), biceps femoris posterior (BF), and obturator internus (OI). Obturator externus (OE), obturator internus (OI), and to a lesser extent gracilis (GR), biceps femoris posterior (BF), and semimembranosus (SM) each cross a moment arm of 0° with a negative slope, suggesting they internal rotate the femur in externally rotated positions and externally rotate the femur at internally rotated positions. The only other muscle with a large peak external rotation moment arm was quadratus femoris (QF). Iliacus (ILI) and psoas minor (OMI) both crossed a moment arm of 0° with a positive slope, meaning they function as internal rotators at internally rotated joint angles and as external rotators at externally rotated joint angles.

Comparison between *D. milleri* and *M. domestica*

Hindlimb function was compared between *D. milleri* and *M. domestica* as well as *D. deserti* where muscle moment arm data was available (Figure 14). In all three specimens, moment arm values were scaled to relative femur length (29.8 mm in *D. milleri*, 12.4 mm in *M. domestica*, and 27.0 mm in *D. deserti*) (Rankin *et al.*, 2018). Range of motion about the flexion-extension axis in *M. domestica* was considerably larger than any other rotational axis in either specimen. Most hip flexion and extension moment arms were not considerably different among homologous muscles. Iliotibialis (IT) is an exception to this trend. In *D. milleri*, it has a peak flexion moment arm reaching 1.83 scaled units at 20°, while the flexion moment arm of its homologous muscles, gluteus maximus (GM) and rectus femoris (RF), never reach higher than 0.16 scaled units in both *M. domestica* and *D. deserti*. Iliofibularis (IF) similarly functions entirely as a flexor in *D. milleri* with a peak flexion moment arm of 0.83 scaled units at 20°. However, biceps femoris posterior (BF) acts entirely as an extensor in both *M. domestica* and *D. deserti* with a peak extension moment arm of 0.54 scaled units at -26° in *M. domestica*. Several pairs of homologous muscles show the opposite trend, with extension as the primary function in *D. milleri* and flexion as the primary function in *M. domestica*. These homologous muscle pairs include puboischiofemoralis internus (PIFI) and iliacus (ILI), puboischiofemoralis internus and psoas major (PMA), and psoas minor in *D. milleri* (PMI) with psoas minor in *M. domestica*. Additionally, flexor tibialis internus (FTI) and externus (FTE) have large extensor moment arms in *D. milleri* (peaks at 1.91 and 1.11 scaled units, respectively), while the extension moment arms of semimembranosus (SM) and semitendinosus (ST) are reduced in *M. domestica* (peaks at 0.71 and 0.69 scaled units, respectively) and even more reduced in *D. deserti*.

While functional differences between *D. milleri* and *M. domestica* regarding hip flexion and extension produced mostly tradeoffs between which muscles were contributing to which actions, hip abduction and adduction were both reduced in *M. domestica* compared to *D. milleri*. Ischiotrochantericus (IS), iliofibularis (IF), flexor tibialis internus (FTI), and flexor tibialis externus (FTE) all had consistently large abduction moment arms in *D. milleri* (ranging in abduction moment arm peak from 0.64 to 1.69 scaled units). The homologous muscles in *M. domestica* – obturator internus (OI), gemellus (GE), biceps femoris posterior (BF), semimembranosus (SM),

and semitendinosus (ST) – did not have relatively large abductor or adductor moment arms (maximum abduction moment arm peak among these muscles was 0.34 scaled units). The same trend was found for hip adduction with sartorius (SA), adductor femoris (AF), pubotibialis (PT), and gracilis (GR) each consistently producing large adduction moment arms at all joint angles in *D. milleri* (ranging in adduction moment arm peak from 0.97 to 2.32 scaled units). In *M. domestica*, the homologous muscles – sartorius (SA), adductor brevis (AB), adductor magnus (AM), adductor longus (AL), and gracilis (GR) – each had reduced adduction moment arms at all joint angles (maximum adduction moment arm peak among these muscles was 0.54 scaled units).

Long axis rotation about the hip was overall not considerably different between *D. milleri* and *M. domestica*. The main difference was a slight reduction in external rotation moment arm in *M. domestica* compared to *D. milleri*. Puboischiofemoralis internus (PIFI) and psoas minor (PMI) each had higher external rotation moment arm peaks in *D. milleri* (0.68 and 0.56 scaled units, respectively) than their homologous counterparts in *M. domestica* – pectineus, iliacus, psoas major, and psoas minor (maximum external rotation moment arm peak among these muscles was 0.25 scaled units).

In comparing overall joint function about each axis of the hip, moment arms scaled by femur length were summed for each axis (Figure 15). The same trends observed in individual homologous muscle comparisons were present here. Despite several homologous muscles differing in individual function between *D. milleri* and *M. domestica*, summed flexion-extension moment arms were not different, indicating a restructuring of muscular organization but not of functional mechanical advantage conferred upon the entire joint. Summed abduction and adduction moment arms in *D. milleri* were larger than in *M. domestica* at all joint angles. The primary muscles involved in reduced abductor moment arms were flexor tibialis externus/semitendinosus, flexor tibialis internus/semimembranosus, and iliofibularis/biceps femoris, while the primary muscles involved in reduced adductor moment arms were pubotibialis/adductor longus, gracilis/gracilis, and adductor femoris/adductor brevis and magnus (Figure 16). Summed long axis moment arms demonstrate a slight reduction in external rotation in *M. domestica* compared to *D. milleri* but no change in internal rotation.

Sensitivity Analyses

Two sensitivity analyses were conducted using the *M. domestica* musculoskeletal model to understand how small shifts in parameter values affect functional interpretations. First, hindlimb pose was reconstructed using three neutral poses as references (Figure 17): the stained specimen as it was dissected and scanned, the hindlimb adjusted so that all joint angles were set to 0° rotation (Hutchinson *et al.*, 2005; Charles, Cappellari, Spence, Wells, *et al.*, 2016), and a mid-stance pose based on illustrations of *Didelphis virginiana* (Jenkins, 1971). The moment arm values of most muscles were not altered significantly at most joint angles. However, quadratus femoris (QF) showed increased lateral rotation moment arm in the 0° joint angle pose relative to the dissected pose and decreased lateral rotation moment arm in the mid-stance pose relative to the dissected pose. Gluteus maximus (GM) showed a slight reduction in medial rotation moment arm in the mid-stance pose relative to the dissected pose, though in medially rotated angles (< -30°), it had a slightly higher medial rotation moment arm peak. Adductor longus (AL) showed reduced adduction moment arm in the mid-stance pose relative to the dissected pose. At extremely adducted positions (< 10°), it also showed reduced adduction moment arm values in the 0° joint angle pose relative to the dissected pose. The moment arm values of the rest of the muscles compared among poses showed similar trends.

The second portion of the sensitivity analysis assessed the functional interpretations of small adjustments to muscle attachment site for muscles in *M. domestica* that attach to bones along broad expanses (Figure 18). In obturator externus (OE), changing the coordinates of the muscular attachment site throughout its broad expanse did not affect its function as a lateral rotator, but it did change the magnitude of moment arm throughout the range of motion of the joint. The same change in magnitude was present in adductor longus (AL). For both obturator internus (OI) and biceps femoris posterior (BF), the change in muscle attachment site had relatively little impact on the moment arm plot. Changing muscle attachment site had the largest effect on pectineus (PEC). The proximal muscle origin functioned entirely as a hip extensor, while more distal muscle origins functioned as hip flexors at extended joint angles and as hip extensors at flexed joint angles. The location of the muscle origin for

pectineus changes it from purely a hip extensor to a joint-stabilizer that aids in returning the femur to its position in the neutral pose.

Discussion

In this study, musculoskeletal models of the *Dimetrodon milleri* and *Monodelphis domestica* hindlimb were constructed to investigate functional morphology related to locomotion in basal synapsids and ancestral therian mammals, respectively. Muscle moment arms, which are a proxy for mechanical advantage, were quantified throughout the range of motion of each axis of the hip joint for both specimens. They were contrasted between homologous muscles to better characterize functional tradeoffs during the transition from sprawling to parasagittal gaits in synapsid evolution. These results show that basal synapsids had increased mechanical advantage during sprawling movements (higher abduction-adduction moment arms) while ancestral therian mammals had developed muscles that functioned as joint-stabilizers along a parasagittal axis (negative sloping flexion-extension moment arms that alternate between opposing actions). Parasagittal hindlimbs increase limb support by aligning limbs more closely with the ground reaction force vector (Biewener, 1989, 1990) which may have allowed early diversification in mammalian body size (Dial 2015). Other morphological underpinnings of locomotory function may be reflected in different areas of the musculoskeletal system, as discussed in the following sections.

Transition from sprawling to parasagittal hindlimb posture

"Pelycosaurs", or basal synapsids, are traditionally understood to be sprawling quadrupeds with short limbs sticking out to the side of the body (Romer and Price, 1940; Blob, 2001). This type of stance increases lateral stability when the body is close to the substrate by allowing the limbs to move more freely (Rewcastle, 1983). It is a common stance in scansorial species and is permitted by several bony morphologies, including a deep acetabulum for the femur to be directed outward, sharply bent knees, and a pes turned backward (Gregory

and Camp, 1918; Romer, 1922). However, "pelycosaurs" dominated terrestrial environments during the late Carboniferous and early Permian periods (~300 mya), so the advantages of sprawling locomotion may be remnants of their amniotic ancestors (Benson, 2012). The large body sizes of *Dimetrodon*, *Ophiacodon*, and other basal synapsids indicate an increased need for vertical support (Romer and Price, 1940; Rewcastle, 1983). Strong ventral musculature would have been required to oppose a ground reaction force vector oriented more laterally to the acetabulum (Fröbisch, 2006). It is not surprising that faster, more efficient modes of locomotion would evolve in non-scansorial lineages. As the oldest pelycosaur stratigraphically, it is likely that the ancestral synapsid hindlimb is close morphologically to the hindlimb of *D. milleri* (Benson, 2012), suggesting sprawling gaits were common.

The transition from the sprawling to parasagittal postures is reflected in many of the homologous muscle differences between *D. milleri* and *M. domestica* caused by changes in bony morphology. The most obvious of these differences is the reduction in moment arms of hip adductors (flexor tibialis externus, flexor tibialis internus, and iliofibularis in *D. milleri*; semitendinosus, semimembranosus, and biceps femoris in *M. domestica*) and hip abductors (pubotibialis, gracilis, and adductor femoris in *D. milleri*; adductor longus, adductor brevis, adductor magnus, and gracilis in *M. domestica*) that reduces overall mechanical advantage about this rotational axis in therians compared to basal synapsids (Figure 14). The skeletal changes responsible for decreased moment arms in these muscles include the anterior extension of the ilium and lengthening of the femur, reducing the relative width of the pubo-ischial plate where the hip adductors and abductors attach to the pelvis (Figure 16). The same morphological changes associated with reduced mechanical advantage during sprawling movements (anterior elongation of the ilium and rotation of the femur towards the parasagittal plane through the development of a ball-and-socket femoral head) arose independently in dicynodonts during the Middle Triassic (Fröbisch, 2006) as well as other amniote lineages. Proximo-distal elongation of the femur may be specifically linked to increased running speeds during cursorial locomotion since longer limbs lead to longer stride lengths (Garland and Janis, 1993). During this transition in bony morphology, muscle action about the flexion-extension axis was reorganized so that some flexors became extensors (iliofibularis) or reduced overall extensor function (iliotibialis)

while some extensors became flexors (puboischiofemoralis internus and psoas minor) or reduced overall flexor function (flexor tibialis internus and externus) (Figure 14). However, total flexion-extension leverage about the hip remain unchanged (Figure 15). Furthermore, no muscles in *M. domestica* have hip adduction as their primary function, with the magnitude of the extension moment arm greater in all four muscles with the largest adduction moment arms (Figure 13; AB – adductor brevis, AM – adductor magnus, AL – adductor longus, and GR – gracilis). All of these musculoskeletal changes reflect a shift from sprawling to parasagittal locomotory stances.

In contrast with non-mammalian synapsids, the earliest mammals (including multituberculates) had expanded ecological scope, occupying terrestrial, arboreal, and scansorial landscapes (Polly, 2007). The evolution of a more parasagittal stance is thought to be an ancestral condition for therians and not the ancestral state of all mammals (Polly, 2007). The ecological diversification of multituberculates is related to the development of improved feeding mechanics (Wilson *et al.*, 2012), which preserves parasagittalism as a precursor for global dispersal in therian mammals as a viable hypothesis. Muscle synapomorphies of the hindlimb are consistent with this tempo of transition in therians, with more differences between the last common ancestor (LCA) of all mammals and the LCA of therians than between the LCA of therians and the LCA of placentals (Diogo *et al.*, 2016). The modern opossum, which has been described as a plesiomorphic representation of basal therians (Jenkins, 1971; Argot, 2001), is therefore an ideal model for interpreting the functional morphology of the ancestral therian hindlimb. The step cycle of *Didelphis virginiana*, a close relative of *M. domestica*, includes a maximum angle of 35° between the femur and the parasagittal plane, which is drastically reduced compared to *D. milleri* where the femur extends almost directly outward (Jenkins, 1971). In this study, *Monodelphis domestica* showed reduced moment arms along the abduction-adduction axis compared to its synapsid ancestors (Figure 15), suggesting sprawling movements would require more muscular contractile force to produce the same action and are therefore less energetically efficient. Furthermore, *M. domestica* has several muscles that act as joint stabilizers about the flexion-extension axis of the hip (pectineus, obturator externus, gemellus, rectus femoris, sartorius, adductor brevis, and adductor longus), indicating a tendency to return the femur towards the neutral

pose rather than pushing away (Young, Scott and Loeb, 1993). *D. milleri* had no muscles with this parasagittal joint-stabilizing function (Figure 14).

While the transition from sprawling to parasagittal postures reduces overall mechanical advantage of the hip joint due to decreased leverage, musculoskeletal traits elsewhere in the body could have evolved more efficient modes of movement in the lineage leading to therians. At slow walks and trots, slight lateral bending of the trunk is apparent in *M. domestica* as well as *Felis catus* and even in some lepidosaurians indicating its ancestral presence in quadrupeds, but sagittal bending only occurs during the half-bound and other galloping movements of mammals (Pridmore, 1992). The internal organization of the mammalian respiratory system also has increased energy production capacity compared to reptiles, including larger organs with more mitochondria and greater membrane surface area for metabolic activity (Else and Hulbert, 1981; Garland, 1994). While sprawling movements in basal synapsids are associated with increased mechanical advantage during abducted and adducted rotations of the femur, upright postures decrease mass-specific muscle force during parasagittal movement by aligning limbs more closely with the ground reaction force vector (Biewener, 1989, 1990). Modern mammals are also characterized by longer limbs (Polly, 2007), which are evident in the *M. domestica* model, and together with increased flexion-extension range of motion would produce longer stride lengths. These musculoskeletal performance changes in therians reduce overall energy expenditure during locomotion, allowing faster and prolonged movements at equal body sizes. Hindlimbs located underneath the body also increase vertical support, decreasing stress on the skeletal system and allowing for expanded variation in body size in therians (Dick and Clemente, 2017). Reducing energy expenditure of the hindlimb may also allow for increased functionality of the forelimb, which in *M. domestica* is adapted for grasping small prey and climbing (Argot, 2001). These changes in locomotory efficiency together with the increased range of body sizes of therians support the idea that ecological diversification followed morphological transitions during synapsid evolution.

Sensitivity analyses

During the construction of the *M. domestica* musculoskeletal model, the neutral pose was determined by leaving the muscles as positioned during scanning (Figure 3). Previously, neutral poses have been established during model construction by reducing all joint angles to 0° (Hutchinson *et al.*, 2005; Charles, Cappellari, Spence, Hutchinson, *et al.*, 2016; Goh *et al.*, 2017). Manipulating the model orientation from dissected poses to this 0° joint angle pose does not increase the comparability of muscle function across taxa since the limbs of each individual will have to be rotated to different extents to produce the same pose. Aside from not solving the issue of comparability, it may produce kinematically inviable postures where osteological structures pass through each other. While this method may allow for comparisons between vertebrates with near-identical postures and gaits, it does not allow for broad, comparative studies over evolutionary timescales. Despite these issues, leaving the limbs oriented in the same posture as scanned does not ensure postures are comparable among taxa. It also creates difficulty in comparing extant taxa where soft tissue scans are possible to extinct taxa known only from skeletal remains. This problem of neutral pose orientation is confirmed in the *M. domestica* model in this study which shows that varying neutral pose does affect biomechanical interpretation of some muscles (Figure 17) as has been shown previously (Hutchinson, 2004a, 2004b). These shifts in functional interpretation include the quadratus femoris (QF) and adductor longus (AL) which alter moment magnitude with the mid-stance pose typically conferring reduced mechanical advantage but showing the same overall functional trend. Only in quadratus femoris did the mid-stance pose also shift in function from external to internal rotation at internally rotated joint angles, suggesting that at certain stages during the step cycle, it may become an internal rotator. This information would have been lost during interpretation of the model if this pose was not reconstructed.

Further sensitivity analysis of the *M. domestica* model illustrate that broad muscles may confer different functional advantages through different lines of action (Figure 18). Choosing an appropriate muscle attachment site may also alter the magnitude of the moment arm, as can be seen in obturator externus (OE) and adductor longus (AL). In pectineus (PEC), the location of the muscle attachment site in the model changes whether the muscle is classified simply as a hip extensor at all joint angles or as a joint-stabilizing muscle that switches to a

flexor at extended joint angles. It is possible that the muscle provides both actions, as hip extensor and as intrinsic hip stabilizer, but again this information would have been lost without the placement of multiple attachment sites for broad muscles. Functional understanding of the postural transition from synapsids to therians does not depend solely on the interpretation the muscles with altered function in these sensitivity analyses, so despite these issues, the general trends in locomotory potential observed in this study are upheld.

Conclusions

The methods used to create the musculoskeletal models here for *D. milleri* and *M. domestica* support a transition from sprawling to parasagittal gaits reflected in the functional morphology of the proximal hindlimb. In basal synapsids, the femur pointed outward from the body and operated primarily on a horizontal plane. This sprawling movement was aided by strong ventral musculature and large abduction-adduction moment arms about the hip, but it created body size constraints by limiting vertical support and increasing stress on the skeletal system. When therapsids appeared, the anterior extension of the ilium and elongation of the femur may have allowed for dual-gait functionality where locomotion could alter between sprawling and parasagittal gaits (Fröbisch, 2006; Kemp, 2006). The reduction in mechanical advantage about the adduction-abduction axis is likely associated with the increasingly parasagittal stance of the hindlimb found in therians. In conjunction with improved metabolic capability and adaptations of the vertebral column, the elongation of the femur allowed for increased speeds during cursorial locomotion while the forelimbs evolved grasping mechanics for catching prey and climbing. The development of joint-stabilizing muscles about the flexion-extension axis in *M. domestica* also suggests parasagittal stances in basal therians would have been supported by hindlimb muscle function.

The sensitivity analyses conducted here agree with previous studies in demonstrating the need for improved model-building methods, including consistency in positioning the reference pose for functional comparisons and including muscle-specific properties like accounting for broad bony attachments. Altering model-building parameters do not affect overall functional interpretation in the *D. milleri* and *M. domestica* specimens from this study, so the general comparisons between basal synapsids and the ancestral therian

condition are not hindered by these methodological issues. The musculoskeletal models produced here are useful tools for research evaluating the evolution of mammalian locomotion. They further provide a framework for adding transitional species to investigate the specific sequence of morphological and biomechanical changes during this transition as well as the overall rate and drivers of phenotypic evolution in synapsids.

Acknowledgements

I would like to thank Stephanie E. Pierce for directly supervising this project at Harvard University and Rampal Etienne for supervising this project externally from the University of Groningen. Thank you as well to the entire Pierce Lab at Harvard for thought-provoking discussions about musculoskeletal modeling and in particular to Phil Lai and Sophie Regnault for teaching me how to use different methodologies and software. I would also like to thank my fellow MEME students for making this program an unforgettable experience from start to finish. Lastly, this project would not have been possible without the incredible organizers and administrators of MEME who help so many young scientists find their niche in evolutionary biology.

References

Argot, C. (2001) ‘Functional-adaptive anatomy of the forelimb in the Didelphidae, and the paleobiology of the Paleocene marsupials Mayulestes ferox and Pucadelphys andinus’, *Journal of Morphology*, 247, pp. 51–79. doi: 10.1002/1097-4687(200101)247:1<51::AID-JMOR1003>3.0.CO;2-#.

Bates, K. T. and Falkingham, P. L. (2012) ‘Estimating maximum bite performance in Tyrannosaurus rex using multi-body dynamics’, *Biology Letters*, 8(4), pp. 660–664. doi: 10.1098/rsbl.2012.0056.

Benson, R. B. J. (2012) ‘Interrelationships of basal synapsids: Cranial and postcranial morphological partitions suggest different topologies’, *Journal of Systematic Palaeontology*, 10(4), pp. 601–624. doi: 10.1080/14772019.2011.631042.

Biewener, A. (1990) ‘Biomechanics of mammalian terrestrial locomotion’, *Science*, 250(4984), pp. 1097–1103. doi: 10.1126/science.2251499.

Biewener, A. A. (1989) ‘Scaling body support in mammals: Limb posture and muscle mechanics’, *Science*, 245(4913), pp. 45–48. doi: 10.1126/science.2740914.

Blob, R. W. (2001) ‘Evolution of hindlimb posture in nonmammalian therapsids: biomechanical tests of paleontological hypotheses’, *Paleobiology*, 27(1), pp. 14–38. doi: 10.1666/0094-8373(2001)027<0014:EOHPIN>2.0.CO;2.

Brassey, C. A., Maidment, S. C. R. and Barrett, P. M. (2017) ‘Muscle moment arm analyses applied to vertebrate paleontology: a case study using Stegosaurus stenops Marsh, 1887’, *Journal of Vertebrate Paleontology*, 37(5). doi: 10.1080/02724634.2017.1361432.

Brinkman, D. (1980) ‘The hind limb step cycle of *Caiman sclerops* and the mechanics of the crocodile tarsus and metatarsus’, *Canadian Journal of Zoology*, 58(12), pp. 2187–2200. doi: 10.1139/z80-301.

Burkholder, T. J. and Nichols, T. R. (2004) ‘A Three Dimensional Model of the Feline Hindlimb Thomas’, *Journal of Morphology*, 261(1), pp. 118–129. doi: 10.1016/j.actbio.2009.04.013.Role.

Campione, N. E. and Evans, D. C. (2012) 'A universal scaling relationship between body mass and proximal limb bone dimensions in quadrupedal terrestrial tetrapods', *BMC Biology*, 10. doi: 10.1186/1741-7007-10-60.

Charles, J. P., Cappellari, O., Spence, A. J., Wells, D. J., *et al.* (2016) 'Muscle moment arms and sensitivity analysis of a mouse hindlimb musculoskeletal model', *Journal of Anatomy*, 229(4), pp. 514–535. doi: 10.1111/joa.12461.

Charles, J. P., Cappellari, O., Spence, A. J., Hutchinson, J. R., *et al.* (2016) 'Musculoskeletal geometry, muscle architecture and functional specialisations of the mouse hindlimb', *PLoS ONE*, 11(4), pp. 1–21. doi: 10.1371/journal.pone.0147669.

Dial, K. P., Shubin, N., and Brainerd, E. L. (2015). Great transformations in vertebrate evolution. The University of Chicago Press, Ltd., London.

Dick, T. J. M. and Clemente, C. J. (2017) 'Where Have All the Giants Gone? How Animals Deal with the Problem of Size', *PLoS Biology*, 15(1), pp. 1–10. doi: 10.1371/journal.pbio.2000473.

Diogo, R. *et al.* (2016) 'Comparative Myology and Evolution of Marsupials and Other Vertebrates, With Notes on Complexity, Bauplan, and "Scala Naturae"', *Anatomical Record*, 299(9), pp. 1224–1255. doi: 10.1002/ar.23390.

Diogo, R., Ziermann, J. M., Molnar, J., Siomava, N., & Abdala, V. (2018). Muscles of chordates: Development, homologies and evolution. Oxford, UK: Taylor and Francis.

Else, P. L. and Hulbert, A. J. (1981) 'Comparison of the "mammal machine" and the "reptile machine": energy production.', *The American Journal of Physiology*, 240, pp. R3-9. doi: 10.1152/ajpregu.00549.2003.

Ferner, K., Zeller, U. and Renfree, M. B. (2009) 'Lung development of monotremes: Evidence for the mammalian morphotype', *Anatomical Record*, 292(2), pp. 190–201. doi: 10.1002/ar.20825.

Fröbisch, J. (2006) 'Locomotion in derived dicynodonts (Synapsida, Anomodontia): a functional analysis of the pelvic girdle and hind limb of *Tetragonias njalilus*', *Canadian Journal of Earth Sciences*, 43(9), pp. 1297–

1308. doi: 10.1139/e06-031.

Garland, T. (1994) ‘Ecological Morphology of Locomotor Performance in Squamate Reptiles’.

Garland, T. and Janis, C. M. (1993) ‘Does metatarsal/ femur ratio predicts maximal running speed in cursorial mammals’, *Journal of Zoology*, 229, pp. 133–151.

Goh, C. *et al.* (2017) ‘A 3D musculoskeletal model of the western lowland gorilla hind limb: moment arms and torque of the hip, knee and ankle’, *Journal of Anatomy*, 231(4), pp. 568–584. doi: 10.1111/joa.12651.

Gregory, W. K. and Camp, C. L. (1918) ‘Studies in comparative myology and osteology. No. 3’, *Bulletin of the American Museum of Natural History*, 38(article 15), pp. 447–563. Available at: http://digitallibrary.amnh.org/dspace/handle/2246/1061?mode=full&submit_simple=More+bibliographic+detail+.

Hopson, J. A. (1987) ‘The Mammal-Like Reptiles: A Study of Transitional Fossils’, *The American Biology Teacher*, 49(1), pp. 16–26. doi: 10.2307/4448410.

Hutchinson, J. R. (2004a) ‘Biomechanical modeling and sensitivity analysis of bipedal running ability. I. Extant taxa’, *Journal of Morphology*, 262(1), pp. 421–440. doi: 10.1002/jmor.10241.

Hutchinson, J. R. (2004b) ‘Biomechanical modeling and sensitivity analysis of bipedal running ability. II. Extinct taxa’, *Journal of Morphology*, 262(1), pp. 441–461. doi: 10.1002/jmor.10240.

Hutchinson, J. R. *et al.* (2005) ‘Analysis of hindlimb muscle moment arms in Tyrannosaurus rex using a three-dimensional musculoskeletal computer model: implications for stance, gait, and speed’, *Paleobiology*, 31(4), p. 676. doi: 10.1666/04044.1.

Hutchinson, J. R. *et al.* (2015) ‘Musculoskeletal modelling of an ostrich (*Struthio camelus*) pelvic limb: influence of limb orientation on muscular capacity during locomotion’, *PeerJ*, 3, p. e1001. doi: 10.7717/peerj.1001.

Jenkins, F. A. (1971) ‘Limb posture and locomotion in the Virginia opossum (Didelphis marsupialis) and in other

non-cursorial mammals', *Journal of Zoology*, 165(3), pp. 303–315. doi: 10.1111/j.1469-7998.1971.tb02189.x.

Johnson, W. L. *et al.* (2008) 'A three-dimensional model of the rat hindlimb: musculoskeletal geometry and muscle moment arms', *Journal of Biomechanics*, 41(3), pp. 610–619. doi: 10.1038/jid.2014.371.

Jones, C. L. (1979) 'The morphogenesis of the thigh of the mouse with special reference to tetrapod muscle homologies', *Journal of Morphology*, 162(2), pp. 275–309. doi: 10.1002/jmor.1051620207.

Kemp, T. S. (1978) 'Stance and gait in the hindlimb of a therocephalian mammal-like reptile', *Journal of Zoology*, 186(2), pp. 143–161. doi: 10.1111/j.1469-7998.1978.tb03362.x.

Kemp, T. S. (1980) 'The Primitive Cynodont Procynosuchus: Structure, Function and Evolution of the Postcranial Skeleton', *Philosophical Transactions of the Royal Society B: Biological Sciences*, 288(1027), pp. 217–258. doi: 10.1098/rstb.1980.0001.

Kemp, T. S. 2005. The Origin and Evolution of Mammals. Oxford University Press, Oxford.

Kemp, T. S. (2006) 'The origin and early radiation of the therapsid mammal-like reptiles: A palaeobiological hypothesis', *Journal of Evolutionary Biology*, 19(4), pp. 1231–1247. doi: 10.1111/j.1420-9101.2005.01076.x.

Maidment, S. C. R., Bates, K. T. and Barrett, P. M. (2014) 'Three-Dimensional Computational Modeling of Pelvic Locomotor Muscle Moment Arms in Edmontosaurus (Dinosauria, Hadrosauridae) and Comparisons with Other Archosaurs', *Indiana University Press*, 25, pp. 433–448. Available at: www.jstor.org/stable/j.ctt16gz7wq.31.

Malda, J. *et al.* (2013) 'Of Mice, Men and Elephants: The Relation between Articular Cartilage Thickness and Body Mass', *PLoS ONE*, 8(2), pp. 1–8. doi: 10.1371/journal.pone.0057683.

Maynard Smith, J. and Savage, R. J. G. (1956) 'Some Locomotory Adaptations in Mammals', *Journal of the Linnean Society*.

Meredith, R. W. *et al.* (2011) 'Impacts of the Cretaceous Terrestrial Revolution and KPg Extinction on Mammal Diversification', *Science*, 334(6055), pp. 521–524. doi: 10.1126/science.1211028.

O'Leary, M. a O. *et al.* (2013) 'The Placental Mammal Ancestor and the Post–K-Pg Radiation of Placentals', *Science*, 339(February), pp. 662–667. doi: 10.1126/science.1229237.

Osburn, R. C. (1903) 'Adaptation to Aquatic, Arboreal, Fossorial, and Cursorial Habits in Mammals', *The American Naturalist*, 442.

Pauwels, E. *et al.* (2013) 'An exploratory study of contrast agents for soft tissue visualization by means of high resolution X-ray computed tomography imaging', *Journal of Microscopy*, 250(1), pp. 21–31. doi: 10.1111/jmi.12013.

Payne, R. C. *et al.* (2006) 'Morphological analysis of the hindlimb in apes and humans. II. Moment arms', *Journal of anatomy*, 208, pp. 725–742.

Polly, P. D. (2007) *Limbs in Mammalian Evolution, Fins into Limbs: Evolution, Development, and Transformation*. Chicago: The University of Chicago Press.

Polly, P. D. *et al.* (2016) 'Combining geometric morphometrics and finite element analysis with evolutionary modeling: towards a synthesis', *Journal of Vertebrate Paleontology*, 36(4), pp. 1–23. doi: 10.1080/02724634.2016.1111225.

Pridmore, P. A. (1992) 'Trunk movements during locomotion in the marsupial Monodelphis domestica (didelphidae)', *Journal of Morphology*, 211(2), pp. 137–146. doi: 10.1002/jmor.1052110203.

Rankin, J. W. *et al.* (2018) 'Functional capacity of kangaroo rat hindlimbs : adaptations for locomotor performance'.

Rewcastle, S. C. (1983) 'Fundamental Adaptations in the Lacertilian Hind Limb : A Partial Analysis of the Sprawling Limb Posture and Gait', *Copeia*, 1983(2), pp. 476–487. doi: 10.2307/1444393.

Romer, A. S., and L. I. Price. 1940. Review of the Pelycosauria. Geol. Soc. Am., Spec. Pap., 28:1-538.

Romer, A. S. (1922) 'The locomotor apparatus of certain primitive and mammal-like reptiles', *Bulletin of the American Museum of Natural History*, 46(Vi), pp. 517–606. Available at:

http://scholar.google.com/scholar?hl=en&btnG=Search&q=intitle:The+locomotor+apparatus+of+certain+primitive+and+mammal-like+reptiles#0.

Sargis, E. J. (2002) 'Functional morphology of the forelimb of tupaiids (Mammalia, Scandentia) and its phylogenetic implications', *Journal of Morphology*, 253(1), pp. 10–42. doi: 10.1002/jmor.1110.

Simon, W. H. (1970) 'Scale effects in animal joints. I. Articular cartilage thickness and compressive stress.', *Arthritis and rheumatism*, 13(3), pp. 244–256.

Springer, M. S. *et al.* (2013) 'Technical Comment on "The Placental Mammal Ancestor and the Post–K-Pg Radiation of Placentals"', *Science*, 613–b(August). doi: 10.1126/science.1229237.

Williams, S. B., Payne, R. C. and Wilson, A. M. (2007) 'Functional specialisation of the thoracic limb of the hare (Lepus europeus)', *Journal of Anatomy*, 210, pp. 472–490. doi: 10.1111/j.1469-7580.2007.00703.x.

Wilson, G. P. *et al.* (2012) 'Adaptive radiation of multituberculate mammals before the extinction of dinosaurs', *Nature*. Nature Publishing Group, 483(7390), pp. 457–460. doi: 10.1038/nature10880.

Witmer, L. M. (1995) 'The Extant Phylogenetic Bracket and the importance of reconstructing soft tissues in fossils', in Thomason, J. (ed.) *Functional morphology in vertebrate paleontology*. Cambridge University Press.

Young, R. P., Scott, S. H. and Loeb, G. E. (1993) 'The distal hindlimb musculature of the cat: multiaxis moment arms at the ankle joint R.P.', *Experimental Brain Research*, pp. 141–151.

Tables

Table 1.
Specimen identification information and segmentation file properties (Mimics v19) for the species modelled in this study (*Dimetrodon milleri* and *Monodelphis domestica*).

Species	Specimen ID	Type	Region	Width (px)	Height (px)	Pixel Size (mm)	No. Slices
Dimetrodon milleri	MCZ 1365	Fossil	Pelvis	668	1250	0.08429	2000
Dimetrodon milleri	MCZ 1365	Fossil	Femur	718	482	0.07998	2000
Dimetrodon milleri	MCZ 1365	Fossil	Tibia	968	668	0.07998	2000
Dimetrodon milleri	MCZ 1365	Fossil	Fibula	968	668	0.07998	2000
Monodelphis domestica	SEP 36	Stained cadaver	Full body	1560	1537	0.03571	1238

Table 2.
Muscular attachments and abbreviations of the proximal hindlimb muscles in *M. domestica*.

Muscle	Abbr.	Origin	Insertion
Pectineus	PEC	Pubic and ischial rami	Intertrochanteric crest
Iliacus	ILI	Ventral aspect of iliac crest	Lesser trochanter
Psoas major	PMA	Bodies of lower vertebrae, ilium	Lesser trochanter
Psoas minor	PMI	Bodies of lower vertebrae, ilium	Lesser trochanter
Sartorius	SA	Superior iliac spine	Patellar tendon
Rectus femoris	RF	Ilium above the acetabulum	Patellar tendon
Vastus medialis	VM	Medial aspect of proximal femur	Patellar tendon
Vastus lateralis	VL	Lateral aspect of proximal femur	Patellar tendon
Adductor longus	AL	Pubis	Medial aspect of middle femur
Adductor magnus	AM	Caudal pubic ramus	Medial aspect of distal femur
Adductor brevis	AB	Cranial pubic ramus	Medial aspect of middle femur
Gracilis	GR	Caudal pubic ramus	Medial aspect of middle tibia
Gluteus maximus	GM	Lateral iliac crest	Greater trochanter
Gemellus	GE	Ischial spine	Intertrochanteric crest (superior to obturator internus)
Obturator internus	OI	Ischial ramus	Intertrochanteric crest (inferior to obturator externus)
Obturator externus	OE	Body of ischium	Intertrochanteric crest
Quadratus femoris	QF	Caudal pubic ramus	Lateral aspect of middle femur
Caudofemoralis	CA	Ischial tuberosity	Medial femoral condyle
Biceps femoris (anterior)	BFA	Ischial tuberosity	Lateral femoral condyle
Biceps femoris (posterior)	BFP	Ischial tuberosity	Lateral aspect of proximal fibula
Semimembranosus	SM	Ischial tuberosity	Medial aspect of proximal tibia
Semitendinosus	ST	Ischial tuberosity	Medial aspect of middle tibia

Table 3.
Inferred muscular attachment sites and associated inference levels of the proximal hindlimb muscles of *D. milleri* using the Extant Phylogenetic Bracket (EPB) method (Witmer 1995). The EPB used here is illustrated in Figure 6. For each origin (O) and insertion (I) in *D. milleri*, the subsequent parentheses indicate the inference level; L1 = Level 1, L2 = Level 2 (There were no Level 3 inferences). Table 4 provides a summarized version of these attachments.

Urodela	Squamata	Archosauria	Dimetrodon	Monotremata	Marsupialia	Placentalia
M: Puboischiofemoralis internus O: Anterior portion of dorsal midline of puboischiac plate, ypsiloid cartilage, and pubis I: Anterior, dorsal, and ventral faces of femur	M: Puboischiofemoralis internus O: Ischium, pubis, and anterior rim of pubic plate I: Femoral trochanter and posterodorsal margin of proximal femur	M: Puboischiofemoralis internus O: Lumbar vertebrae, sacral ribs, ilium, and ischium I: Proximal femur	*M: Puboischiofemoralis internus* *O: Anterodorsal surface of pubis (L2)* *I: Lesser trochanter (L1)*	M: Pectineus O: Pubis and epipubis I: Femur	M: Pectineus O: Ischium and epipubis I: Femur	M: Pectineus O: Pubic arch and ilium I: Medial ridge of femoral shaft
				M: Iliopsoas O: Lumbar and sacral vertebrae and ilium I: Proximal femur	M: Iliacus O: Ilium I: Femur	M: Iliacus O: Lumbar vertebrae I: Lesser trochanter
					M: Psoas major O: Lumbar and sacral vertebrae I: Femur	M: Psoas major O: Lumbar vertebrae I: Femur
M: Iliocaudalis O: Caudal vertebrae I: Ilium	M: Quadratus lumborum O: Ribs and vertebrae I: Pelvis	M: Quadratus lumborum O: Ribs and vertebrae I: Pelvis	*M: Psoas minor* *O: Sacral ribs and anterodorsal surface of ilium (L2)* *I: Lesser trochanter (L2)*	M: Psoas minor O: Thoracic and lumbar vertebrae and ribs I: Ilium	M: Psoas minor O: Lumbar vertebrae I: Pubis and ischium	M: Psoas minor O: Lumbar vertebrae I: Ilium
M: Puboischiofemoralis externus O: Ventral midline and anterior border of puboischiac plate, pubis, and ischium I: Femoral crest, femoral shaft distal to crest, and femoral trochanter	M: Puboischiofemoralis externus O: Pubis and ischium I: Intertrochanteric fossa and internal trochanter of femur	M: Puboischiofemoralis externus O: Pubis, ischium, and last abdominal rib I: Proximal femur	*M: Puboischiofemoralis externus* *O: Ventral surface of puboischium below the acetabulum (L1)* *I: Intertrochanteric fossa of femur (L1)*	M: Obturator externus O: Hip bone I: Proximal femur	M: Obturator externus O: Pubis and ischium I: Femur	M: Obturator externus O: Margin of obturator foramen I: Femur
				M: Quadratus femoris O: Ischium I: Proximal femur	M: Quadratus femoris O: Ischium I: Femur	M: Quadratus femoris O: Ischium I: Femur
M: Ischiotrochantericus O: Lateral and dorsal surfaces of puboischiac plate I: Tuberosity on posterior side of femoral head	M: Ischiotrochantericus O: Ischial tuberosity and posterior surface of ischium I: Proximal femur	M: Ischiotrochantericus O: Ischium I: Proximal femur	*M: Ischiotrochantericus* *O: Posterodorsal surface of ischium (L1)* *I: Posterior trochanter of femur (L2)*	M: Ischiotrochantericus O: Ischium I: Proximal femur	M: Obturator internus O: Ischium and pubis I: Femur	M: Obturator internus O: Medial surface of ischium I: Trochanteric fossa
					M: Gemellus O: Ischium I: Femur	M: Gemellus O: Ischium I: Trochanteric fossa
M: Extensor iliotibialis O: Ilium I: Wide tendon inserting onto crista tibialis	M: Iliotibialis O: Broad aponeurosis from lateral surface of ilium I: Cnemial crest of tibia	M: Iliotibialis O: Ilium I: Tibia	*M: Iliotibialis* *O: Anterolateral surface of ilium (L1)* *I: Tibial tuberosity (L1)*	M: Gluteus maximus O: Sacral vertebrae I: Proximal femur	M: Gluteus maximus O: Sacral and caudal vertebrae I: Femur	M: Gluteus maximus O: Ilium and vertebrae I: Femur
				M: Rectus femoris O: Ilium I: Patella, tibia	M: Rectus femoris O: Ilium I: Patella, tibia	M: Rectus femoris O: AIIS and border of acetabulum I: Patella, tibia
	M: Femorotibialis O: Entire length of femoral shaft I: Iliotibial tendon	M: Femorotibialis O: Femur I: Tibia	*M: Femorotibialis* *O: Dorsal surface of proximal femur (L2)* *I: Tibial tuberosity (L1)*	M: Vastus medialis O: Femur I: Patella, tibia	M: Vastus medialis O: Femur I: Patella, tibia	M: Vastus medialis O: Neck and proximal femoral shaft I: Patella, tibia
				M: Vastus lateralis O: Femur I: Patella, tibia	M: Vastus lateralis O: Femur I: Patella, tibia	M: Vastus lateralis O: G. and 3rd trochanter I: Patella, tibia
	M: Sartorius O: Pubis I: Iliotibialis insertion	M: Sartorius O: Ilium, pubis, ischium I: Iliotibialis and gastrocnemius muscles	*M: Sartorius* *O: Ventral ilium ant. to acetabulum (L2)* *I: Tibial tuberosity (L1)*	M: Sartorius O: Pubis I: Tibia	M: Sartorius O: Ilium I: Patella, tibia	

Table 3 (Continued).

Urodela	Squamata	Archosauria	Dimetrodon	Monotremata	Marsupialia	Placentalia
M: Adductor femoris O: Anterior and ventral surface of puboischiac plate I: Ventral face of distal femur	M: Adductor femoris O: Puboischiadic ligament I: Middle 1/3 of femur	M: Adductor femoris O: Ischium I: Femur	***M: Adductor femoris O: Deep ventral surface of pubis (L1) I: Anteroventral surface of distal femur (L1)***	M: Adductor brevis O: Pubis and ischium I: Femur	M: Adductor brevis O: Pubis I: Femur	M: Adductor brevis O: Pubis and ischium I: Femur
				M: Adductor magnus O: Pubis and ischium I: Femur	M: Adductor magnus O: Pubis and ischium I: Femur	M: Adductor magnus O: Pubis and ischium I: Femur
M: Pubotibialis O: Anterolateral border of puboischiac plate I: Proximal tibia	M: Pubotibialis O: Pubis I: Tibia		***M: Pubotibialis O: Pubic tubercle (L2) I: Ventral surface of proximal tibia (L2)***	M: Adductor longus O: Pubis I: Femur	M: Adductor longus O: Pubis and ischium I: Femur	M: Adductor longus O: Pubis I: Femoral shaft
M: Gracilis O: Ventral midline of puboischiac plate I: Proximal 2/3 of anteromedial tibia	M: Gracilis O: Region surrounding ischiopubic ligament I: Proximal aspect of tibial shaft	M: Gracilis O: Ischium I: Tibia	***M: Gracilis O: Superficial ventral surface of pubis (L1) I: Anterior border of proximal tibia (L1)***	M: Gracilis O: Epipubis and ischium I: Tibia	M: Gracilis O: Pubis I: Tibia	M: Gracilis O: Pubic symphysis and ischium I: Cranial and medial tibia and tibial tubercle
M: Iliofibularis O: Extensor iliotibialis tendon I: Posterior border of fibula	M: Iliofibularis O: Posteroventral margin of ilium I: Proximal fibular shaft	M: Iliofibularis O: Ilium I: Fibula	***M: Iliofibularis O: Posterolateral surface of ilium (L2) I: Proximal fibular tubercle (L1)***	M: Biceps femoris O: Ischium I: Patella, tibia	M: Biceps femoris O: Ischium I: Fibula	M: Biceps femoris O: Sacral and caudal vertebrae and sciatic tubercle I: Distal femur and proximal 2/3 of tibia
M: Ischioflexorius O: posterolateral corner of puboischiac plate I: Plantar aponeurosis	M: Flex. tibialis internus O: Anterior iliotibial ligament and posteroventral ischium I: Proximal shaft and posterolateral tibia	M: Flexor tibialis internus O: Ischium I: Tibia	***M: Flex. tibialis int. O: Superficial ventral surface of ischium (L1) I: Anterior border of proximal tibia (L2)***	M: Semimembranosus O: Ischium I: Tibia	M: Semimembranosus O: Ischium I: Tibia	M: Semimembranosus O: Sciatic tuber I: Ridge and medial surface of tibia and fabella
	M: Flexor tibialis externus O: Iliotibial ligament I: Proximolateral tibia	M: Flexor tibialis externus O: Iliac clade I: Gastrocnemius	***M: Flex. tibialis ext. O: Posteroventral surface of ischium (L1) I: Ventral surface of proximal tibia (L1)***	M: Semitendinosus O: Caudal and lumbar vertebrae I: Tibia	M: Semitendinosus O: Ischium I: Tibia	M: Semitendinosus O: Sciatic tuber, sacral and caudal vertebrae I: Medial tibia and tibial tubercle

Table 4.
Muscular attachments and abbreviations of the proximal hindlimb muscles in *D. milleri*.

Muscle	Abbr.	Origin	Insertion
Puboischiofemoralis internus	PIFI	Anterodorsal surface of pubis	Lesser trochanter
Psoas minor	PMI	Sacral ribs and anterodorsal surface of ilium	Lesser trochanter
Puboischiofemoralis externus	PIFE	Ventral surface of pubis and ischium below the acetabulum	Intertrochanteric fossa
Ischiotrochantericus	IS	Posterodorsal surface of ischium	Posterior trochanter
Iliotibialis	IT	Anterolateral surface of ilium	Tibial tuberosity
Femorotibialis	FT	Dorsal surface of proximal femur	Tibial tuberosity
Sartorius	SA	Ventral ilium anterior to acetabulum	Tibial tuberosity
Adductor femoris	AF	Deep ventral surface of pubis	Anteroventral surface of distal femur
Pubotibialis	PT	Pubic tubercle	Ventral surface of proximal tibia
Gracilis	GR	Superficial ventral surface of pubis	Anterior border of proximal tibia
Iliofibularis	IF	Posterolateral surface of ilium	Proximal fibular tubercle
Flexor tibialis internus	FTI	Superficial ventral surface of ischium	Anterior border of proximal tibia
Flexor tibialis externus	FTE	Posteroventral surface of ischium	Ventral surface of proximal tibia

Table 5.
Segment components, origins, and axis orientations for each musculoskeletal model. Axis orientations are indicated by a 3-dimensional coordinate moved 1 mm away from the joint origin in Autodesk 3ds Max along each respective axis in a positive direction.

Segment	Bones	Origin	X-Axis (Cranial)	Y-Axis (Distal)	Z-Axis (Lateral)
D. milleri					
Pelvis	Ilium, ischium, and pubis	Center of acetabulum	(1.0, 0.0, 0.0)	(0.0, 1.0, 0.0)	(0.0, 0.0, 1.0)
Thigh	Femur	Midway between femoral trochanters	(0.818, -0.059, -0.572)	(0.007, 0.996, -0.093)	(0.575, 0.072, 0.815)
Leg	Tibia and fibula	Midway between femoral condyles	(0.728, -0.531, -0.434)	(-0.533, -0.039, -0.846)	(0.433, 0.846, -0.311)
M. domestica					
Pelvis	Ilium, ischium, pubis, and epipubis	Center of acetabulum	(1.0, 0.0, 0.0)	(0.0, 1.0, 0.0)	(0.0, 0.0, 1.0)
Thigh	Femur	Center of femoral head	(-0.082, 0.995, -0.056)	(-0.853, -0.099, -0.513)	(-0.516, 0.006, 0.857)
Leg	Tibia and fibula	Midway between femoral condyles	(-0.090, 0.995, 0.037)	(0.236, 0.057, -0.970)	(-0.968, -0.079, -0.240)

Table 6.
Origin and insertion coordinates in SIMM of muscles used in the *D. milleri* musculoskeletal model. Coordinates represent distance (mm) from the segment origin.

	Origin				Insertion			
Muscle	Segment	x	y	z	Segment	x	y	z
PIFI	Pelvis	51.804	-6.603	-30.056	Thigh	-6.206	8.978	-19.947
PMI	Pelvis	20.560	-11.709	11.972	Thigh	-2.452	10.364	-20.442
PIFE	Pelvis	-19.449	-11.195	-11.716	Thigh	-2.137	14.873	3.023
IS	Pelvis	-59.458	-7.534	-4.759	Thigh	-16.431	9.840	11.822
IT	Pelvis	32.371	0.875	42.774	Leg	3.139	15.111	-12.226
FT	Thigh	8.836	4.840	7.977	Leg	3.139	15.111	-12.226
SA	Pelvis	24.350	-3.596	-10.592	Leg	3.139	15.111	-12.226
AF	Pelvis	36.362	-17.531	-29.723	Thigh	0.898	95.452	-28.733
PT	Pelvis	62.792	-0.522	-43.105	Leg	-7.987	-8.228	-4.970
GR	Pelvis	41.904	-31.179	-41.372	Leg	-9.161	-8.247	-26.836
IF	Pelvis	-28.714	7.967	47.012	Leg	-13.439	23.654	11.328
FTI	Pelvis	-69.494	-20.233	-26.441	Leg	-5.493	-14.741	-16.409
FTE	Pelvis	-62.664	-4.064	-1.648	Leg	-11.031	-3.241	-18.674

Table 7.
Origin and insertion coordinates in SIMM of muscles used in the *M. domestica* musculoskeletal model. Coordinates represent distance (mm) from the segment origin.

	Origin				Insertion			
Muscle	Segment	x	y	z	Segment	x	y	z
Gluteus maximus	Pelvis	-13.852	6.189	8.724	Thigh	0.984	-3.831	0.458
Obturator externus (1)	Pelvis	2.368	1.834	-0.213	Thigh	-0.537	-3.835	-2.029
Obturator externus (2)	Pelvis	5.536	0.377	-1.658	Thigh	-1.514	-3.853	-2.801
Obturator externus (3)	Pelvis	6.971	-1.569	-3.913	Thigh	-3.127	-4.201	-3.704
Obturator internus (1)	Pelvis	5.762	-0.964	-3.19	Thigh	-3.173	-3.49	-4.014
Obturator internus (2)	Pelvis	6.825	-0.987	-5.213	Thigh	-3.173	-3.49	-4.014
Gemellus	Pelvis	1.817	1.438	-0.125	Thigh	0.158	-3.449	-1.023
Quadratus femoris	Pelvis	4.556	2.13	-9.205	Thigh	-6.628	-3.964	-5.837
Adductor magnus	Pelvis	5.198	0.91	-7.695	Thigh	-18.801	-1.955	-11.865
Adductor longus (1)	Pelvis	-1.443	4.144	-8.31	Thigh	-16.663	-3.27	-10.612
Adductor longus (2)	Pelvis	4.177	2.676	-9.272	Thigh	-16.663	-3.27	-10.612
Adductor brevis	Pelvis	-2.126	1.438	-3.673	Thigh	-12.503	-2.467	-8.434
Gracilis	Pelvis	5.625	0.975	-8.497	Leg	1.842	1.596	-10.144
Psoas major	Pelvis	-8.241	3.806	2.583	Thigh	-1.577	-0.885	-4.009
Psoas minor	Pelvis	-15.054	4.856	8.023	Thigh	-2.488	-1.114	-4.064
Iliacus	Pelvis	-14.676	4.582	7.967	Thigh	-1.654	-0.767	-3.11
Pectineus (1)	Pelvis	5.697	0.026	-6.217	Thigh	-0.749	-3.125	-1.67
Pectineus (2)	Pelvis	3.492	2.988	-8.926	Thigh	-0.749	-3.125	-1.67
Pectineus (3)	Pelvis	-2.355	3.202	-6.985	Thigh	-0.749	-3.125	-1.67
Caudofemoralis	Pelvis	4.384	0.819	-1.3	Thigh	-18.896	-2.831	-11.943
Semimembranosus	Pelvis	7.144	-0.929	-5.239	Leg	-0.175	1.644	-3.288
Semitendinosus	Pelvis	7.342	-0.835	-3.758	Leg	1.7	1.589	-7.66
Biceps femoris (anterior)	Pelvis	1.082	1.053	0.95	Thigh	-18.911	-3.807	-11.299
Biceps femoris (posterior) (1)	Pelvis	6.331	-1.136	-2.608	Leg	3.755	-3.247	-1.612
Biceps femoris (posterior) (2)	Pelvis	6.331	-1.136	-2.608	Leg	4.911	-1.616	-8.343
Biceps femoris (posterior) (3)	Pelvis	6.331	-1.136	-2.608	Leg	6.772	-1.483	-14.021
Popliteus	Thigh	-19.97	-4.208	-12.838	Leg	-0.561	1.974	-1.769
Sartorius	Pelvis	-14.464	5.136	8.892	Leg	-2.073	-0.221	-1.657
Vastus medialis	Thigh	-2.278	-1.994	-0.795	Leg	-2.073	-0.221	-1.657
Vastus lateralis	Thigh	-0.88	-3.179	0.992	Leg	-2.073	-0.221	-1.657
Rectus femoris	Pelvis	-1.882	0.084	0.648	Leg	-2.073	-0.221	-1.657

Table 8.
Joint ranges of motion for each musculoskeletal model determined by rotating each segment from its position in the neutral pose until it collided with another bony structure.

Specimen	Joint	Axis of Rotation	Minimum of Range	Maximum of Range	Total Range of Motion
D. milleri	Hip	X-Axis (Flexion-Extension)	-65°	20°	85°
		Y-Axis (Long axis rotation)	-55°	40°	95°
		Z-Axis (Abduction-Adduction)	-20°	50°	70°
	Knee	X-Axis (Flexion-Extension)	-10°	25°	35°
		Y-Axis (Long axis rotation)	-10°	10°	20°
		Z-Axis (Abduction-Adduction)	-5°	5°	10°
M. domestica	Hip	X-Axis (Flexion-Extension)	-60°	80°	140°
		Y-Axis (Long axis rotation)	-50°	20°	70°
		Z-Axis (Abduction-Adduction)	-5°	75°	80°
	Knee	X-Axis (Flexion-Extension)	-80°	80°	160°
		Y-Axis (Long axis rotation)	-10°	0°	10°
		Z-Axis (Abduction-Adduction)	0°	0°	0°

Table 9.
Properties of wrapping objects placed into the *D. milleri* SIMM model. Muscle abbreviations are listed in Table 4.

Location	Segment	Muscle(s) Affected	Rotation (x, y, z)	Translation (x, y, z) (mm)	Radius (mm)	Height (mm)
Cylinders						
Pubis	Pelvis	PIFI	(17.09, -53.78, 43.93)	(39.93, -4.27, -27.04)	6.0	30.0
Ridge of puboischium	Pelvis	PMI	(0.0, 0.0, 0.0)	(23.0, -5.5, 4.0)	6.0	30.0
Ischium	Pelvis	IS	(-56.22, -75.47, -80.46)	(-43.64, -8.20, -0.79)	4.0	18.0
Ridge of acetabulum	Pelvis	PIFE	(-6.62, -21.64, 127.09)	(-13.36, -6.06, -2.32)	8.0	20.0
Proximal femur	Thigh	PMI	(-47.94, 3.97, 41.80)	(5.97, 0.37, -7.14)	12.0	25.0
Lesser trochanter of femur	Thigh	PIFI	(84.28, -25.60, -81.42)	(0.52, 5.0, -12.25)	10.0	15.0
Ellipsoids					*(x, y, z)*	
Pubis	Pelvis	AF	(-86.96, -5.30, 116.27)	(27.87, -5.96, -24.23)	(8.0, 30.0, 10.0)	-
Proximal femur	Thigh	IT, SA	(65.92, 16.49, 35.20)	(4.49, 3.92, -0.08)	(12.0, 22.0, 18.0)	-
Distal femur	Thigh	AF, PT	(-57.19, -54.01, 163.65)	(3.40, 87.67, -23.24)	(6.0, 12.0, 6.0	-

Table 10.
Properties of wrapping objects placed into the *M. domestica* SIMM model. Muscle abbreviations are in Table 2.

Location	Segment	Muscle(s) Affected	Rotation (x, y, z)	Translation (x, y, z) (mm)	Radius (mm)	Height (mm)
Cylinders						
Epipubis	Pelvis	AL1	(61.46, 25.76, -103.59)	(-3.75, 3.11, -6.25)	0.5	2.5
Ridge of acetabulum (ilium)	Pelvis	PMI, ILI	(-133.40, -12.62, 119.41)	(-2.29, 0.68, -1.33)	1.0	2.0
Ridge of acetabulum (cranial)	Pelvis	AM, AL2, AB, GR, PMA	(-113.71, -30.83, 120.40)	(-2.17, 1.15, -2.01)	1.5	3.8
Ischium	Pelvis	OE1, OE2, GE, CA	(-31.36, -60.16, -61.39)	(3.06, 0.67, -1.41)	0.65	5.0
Shaft of femur (ventral)	Thigh	QF	(86.66, 21.12, -69.09)	(-4.38, -2.98, -4.48)	0.5	2.0
Femoral condyles	Thigh	SA, VM, VL, RF	(90.0, 0.0, 160.0)	(-20.74, -2.50, -12.50)	1.8	4.0
Spheres						
Head of femur	Thigh	GM, OE1, GE, BFA	(90.0, -0.0, 75.0)	(0.00, -0.20, -0.03)	1.4	-
Greater trochanter of femur	Thigh	GM	(71.68, -24.18, 51.04)	(-0.23, -3.39, 0.21)	1.25	-
Ellipsoids					*(x, y, z)*	
Ischial ramus	Pelvis	BFP	(-51.38, -63.04, -139.68)	(6.22, -0.95, -3.16)	(0.5, 0.5, 2.0)	-
Torii					*(outer)*	*(inner)*
Neck of femur (dorsal)	Thigh	GM	(-74.31, -89.47, 129.04)	(-1.99, -1.82, 2.32)	0.3	2.5
Neck of femur (ventral)	Thigh	CA, BFA	(139.17, -52.36, -167.57)	(3.46, -6.57, -2.37)	0.25	2.5
Hip extensors	Thigh	SM, ST, BFP	(-19.06, 58.43, -161.84)	(-0.30, -2.07, -9.67)	0.2	3.0

Figures

Figure 1.
Synapsid phylogeny with representative groups along the transition from sprawling to parasagittal gaits. The two species modelled in this project (*Dimetrodon milleri* and *Monodelphis domestica*), labelled and highlighted, represent the basal synapsid and ancestral mammal condition, respectively. Comparing musculoskeletal function between *D. milleri* and *M. domestica* illustrates the shift in overall locomotory capability during this transition.

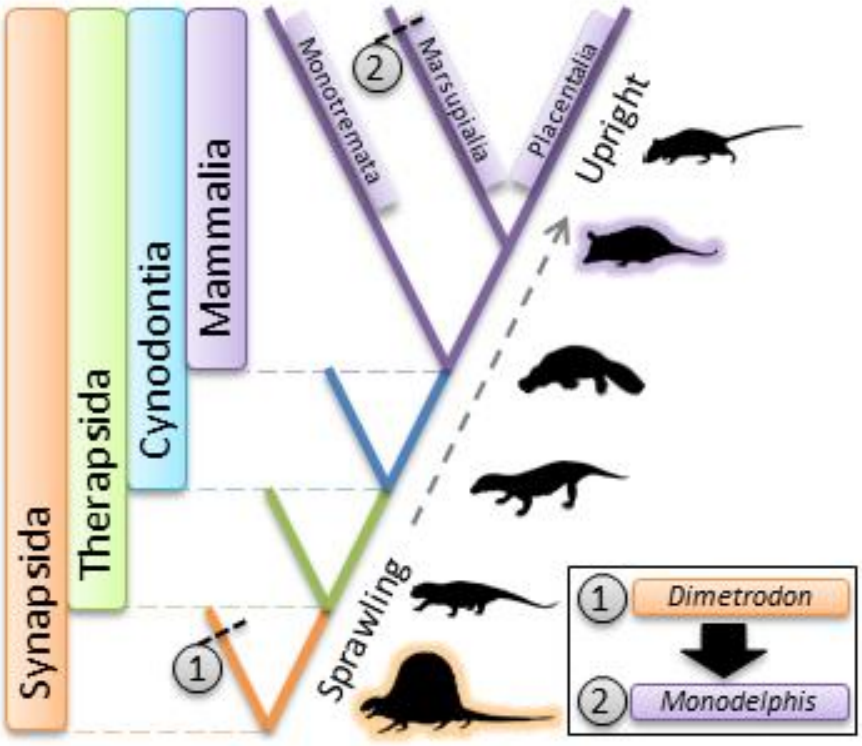

Figure 2.
Three-dimensional reconstruction of microcomputed tomography (μCT) scans of the *D. milleri* (MCZ 1365) hindlimb bones using Mimics v19. From left to right: pelvis, femur, tibia, and fibula; from top to bottom: dorsal and ventral views. Scan details are recorded in Table 1.

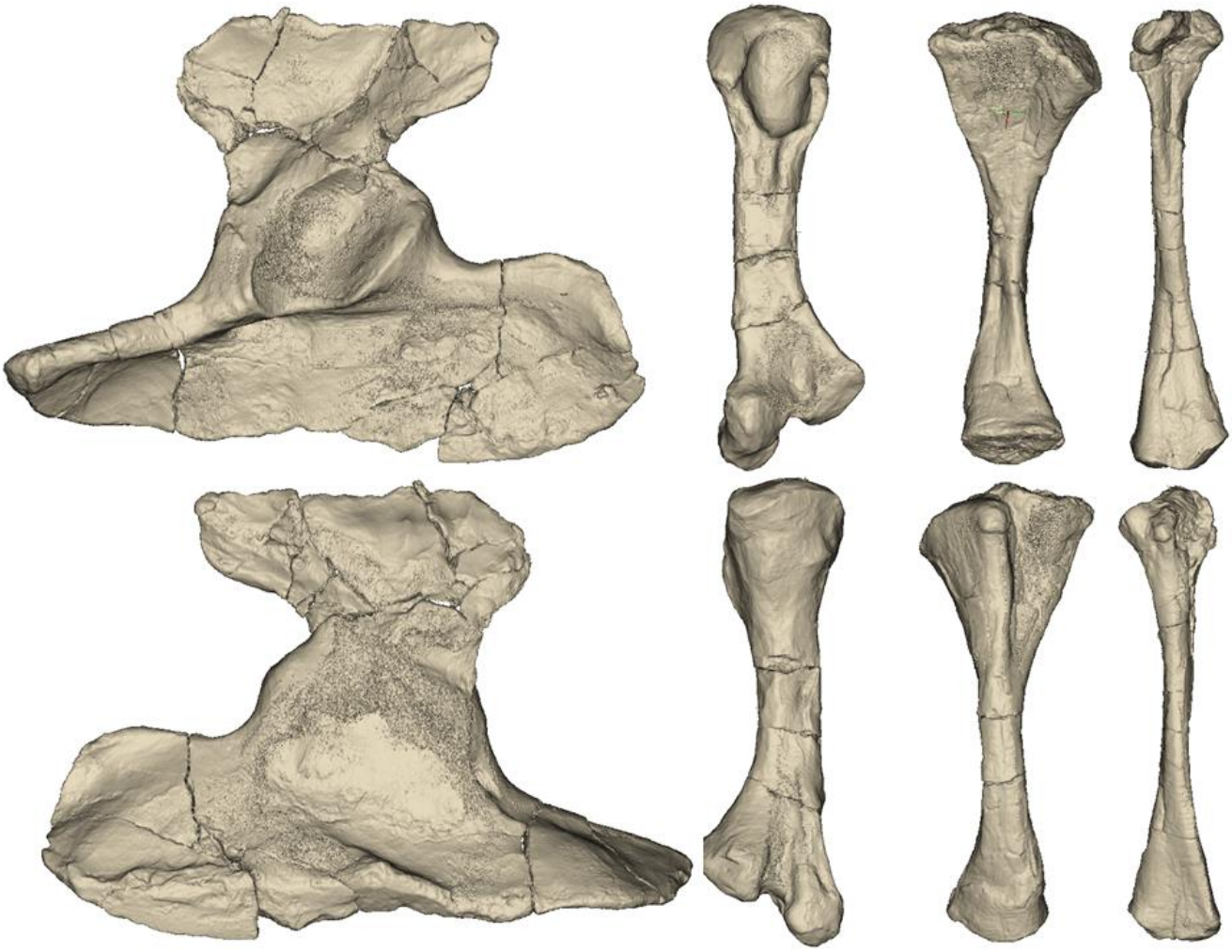

Figure 3.
Three-dimensional reconstruction of μCT scans of the *M. domestica* specimen (SEP 36) in Mimics v19 following an 8-week stain in phosphomolybdic acid (PMA). Top: skeletal system only; bottom: combined musculoskeletal system. The left hindlimb is indicated by the red box in both images.

Figure 4.
Three-dimensional reconstruction of superficial (top) and deep (bottom) muscles of the proximal *M. domestica* hindlimb following staining and digital segmentation. Left: medial; right: lateral. For muscle abbreviations, see Table 2.

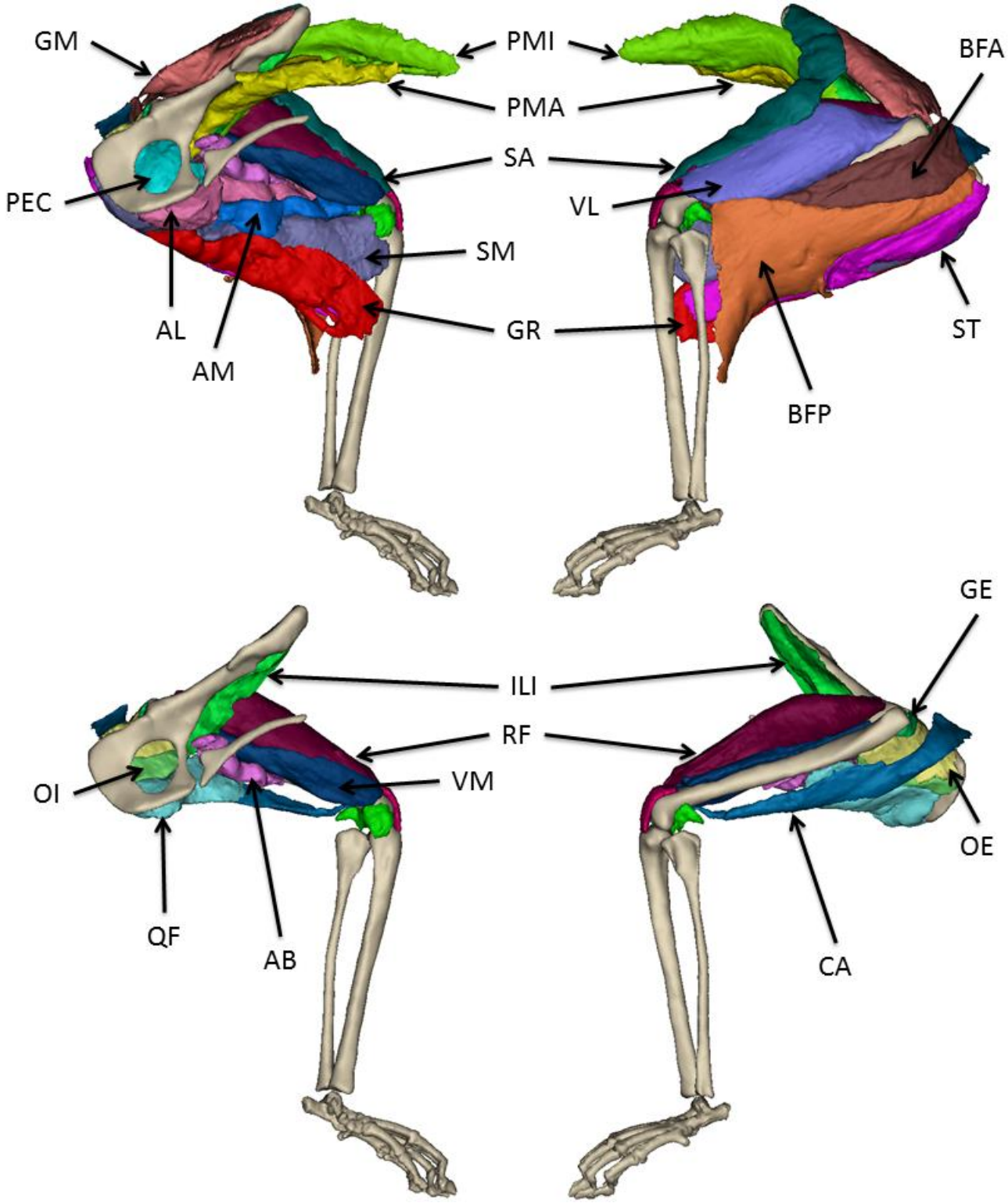

Figure 5.
The extant phylogenetic bracket (EPB) method compares soft tissue anatomy and their osteological correlates (OCs) in extant outgroup species to infer muscular attachments in extinct species (Witmer 1995). This method requires at least two outgroup species: one sister group to the fossil species (A, below) and one sister group to the clade formed by the first pair (C, below). Level I Inference: the soft tissue (in this case, muscular attachment) has the same OC in both A and C, and the OC is identifiable in B. Level II Inference: either A or C has the same OC as B, but not both. Level III Inference: the OCs of A and C are not identifiable in B.

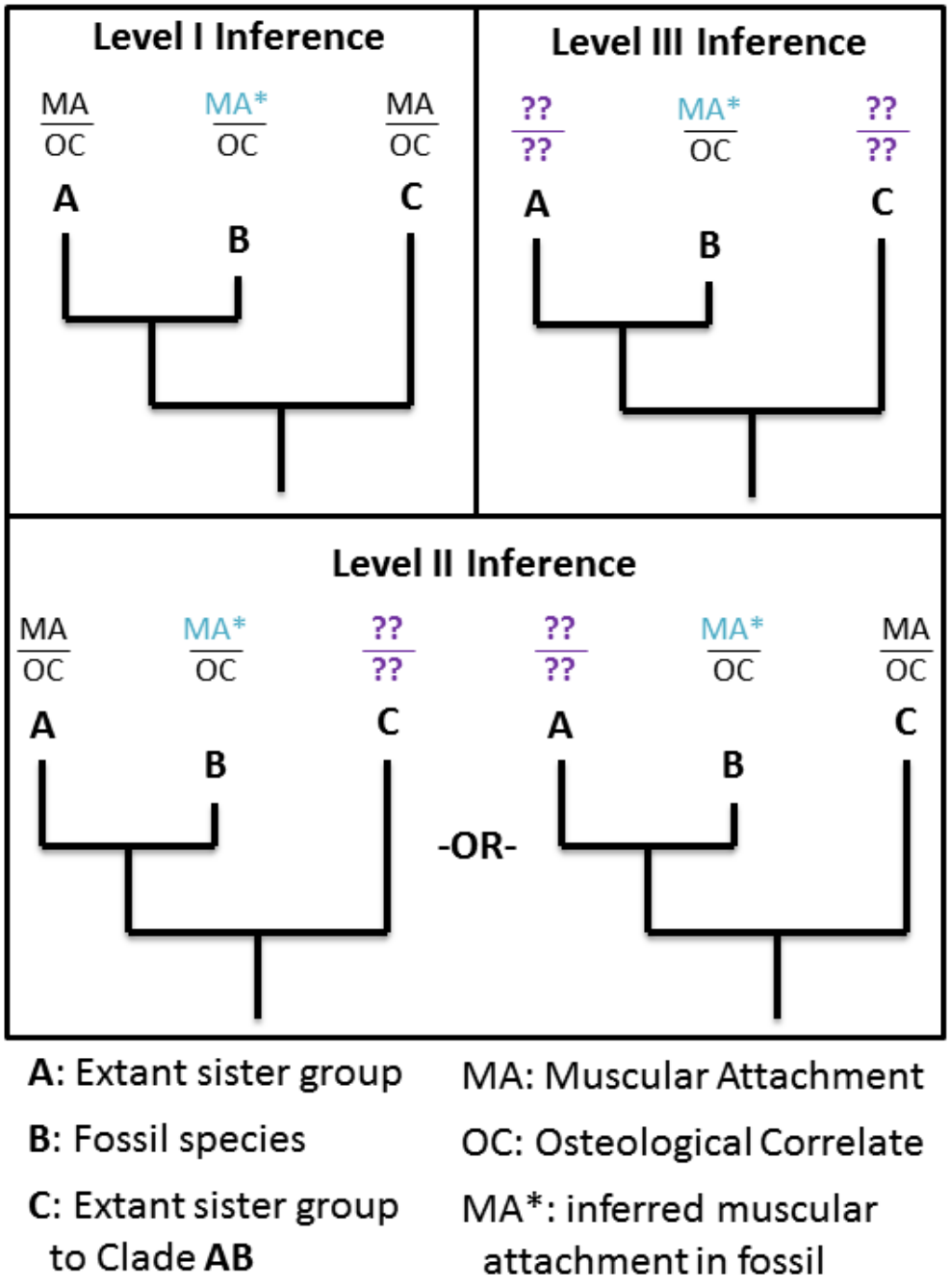

Figure 6.
The extant phylogenetic bracket (EPB) used to infer muscular attachment sites in *D. milleri* (Table 3) *sensu* Witmer 1995. There are three extant sister groups to *D. milleri* (Monotremata, Marsupialia, and Placentalia; Figure 5 – "A") and three extant sister groups to the clade formed by the former (Urodela, Squamata, Archosauria; Figure 5 – "C"). Inferences were made based on the presence of the same osteological correlate and corresponding soft tissue structure in at least one outgroup from "A" and one outgroup from "C".

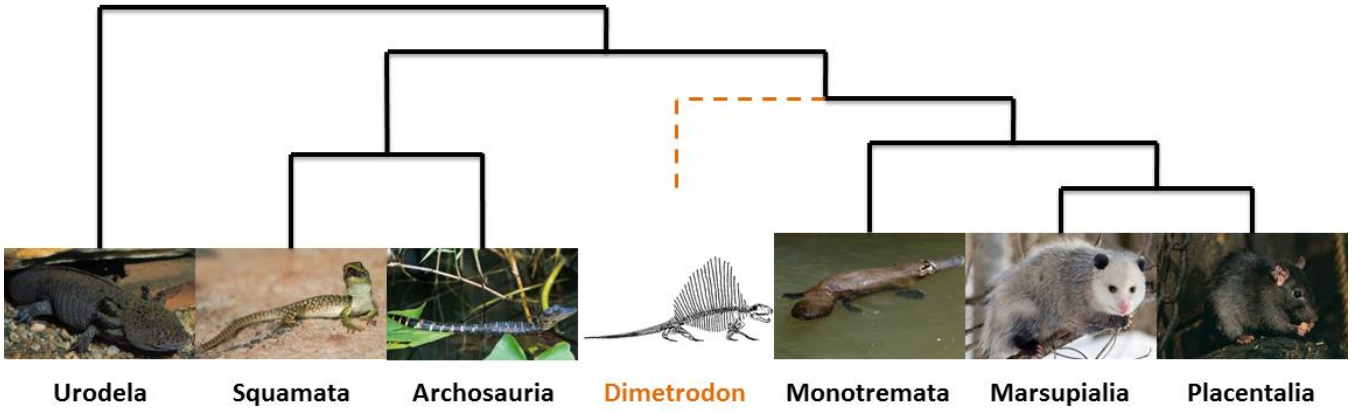

Figure 7.
The inferred muscular attachments of the 13 proximal hindlimb muscles of *D. milleri* using the extant phylogenetic bracket (EPB) method. Red indicates muscle origins and blue indicates muscle insertions. From left to right: pelvis, femur, tibia, and fibula; from top to bottom: dorsal and ventral views. For muscle abbreviations, see Table 4.

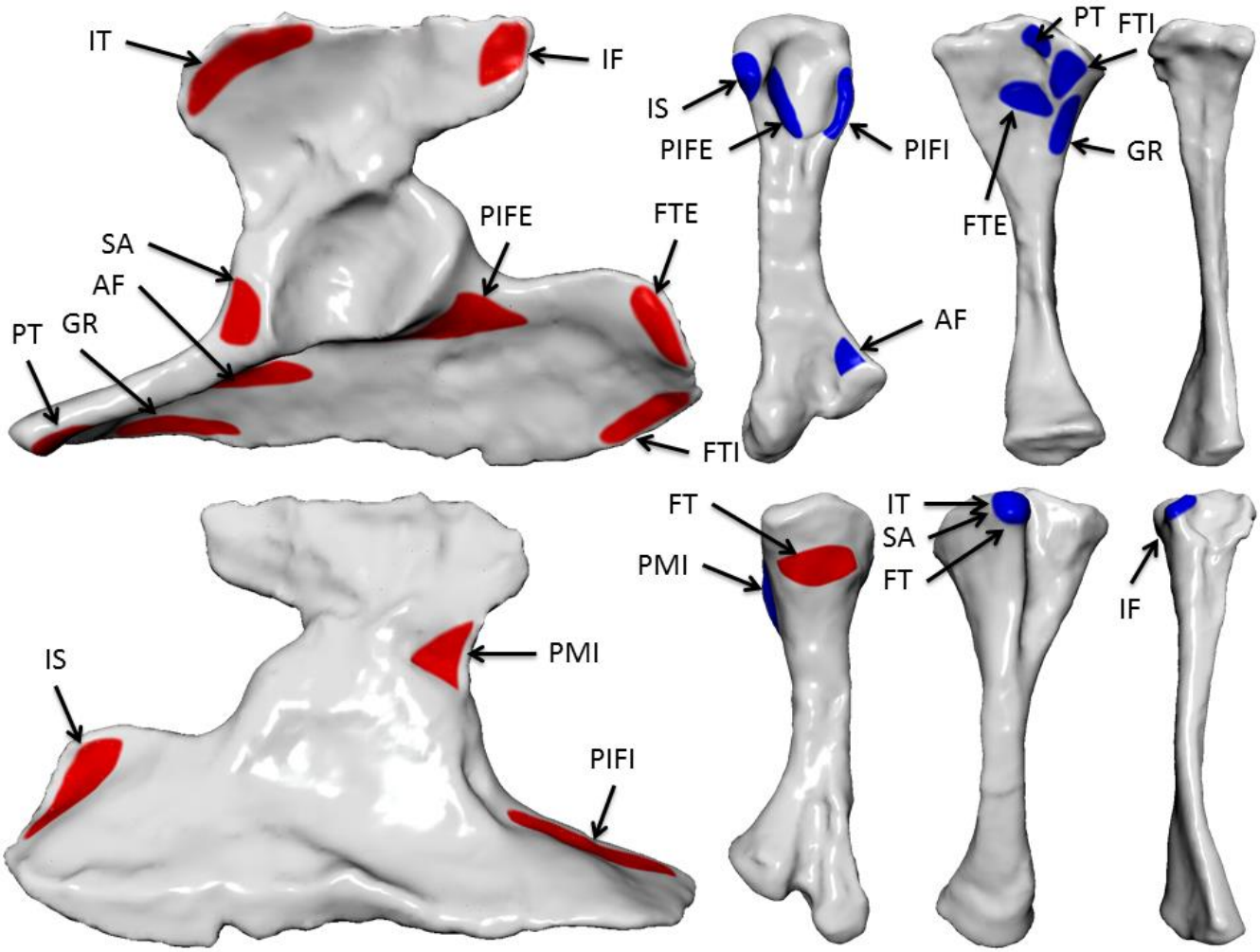

Figure 8.
Joint spacing in *D. milleri* was determined in three steps following established scaling relationships in the literature: (top) stylopodial circumference scales with body mass in quadrupedal terrestrial tetrapods (Campione 2012), (middle) body mass scales with femoral condyle (FC) cartilage thickness in therian mammals (Malda 2013), and (bottom) knee cartilage thickness scales with hip cartilage thickness in placental mammals (Simon 1970). Colors indicate study: *Campione 2012* (black), *Malda 2013* (green), and *Simon 1970* (blue). In all three plots, *D. milleri* is labeled by the red square. Units are kept at the original scale used in each study and are therefore not equivalent between plots.

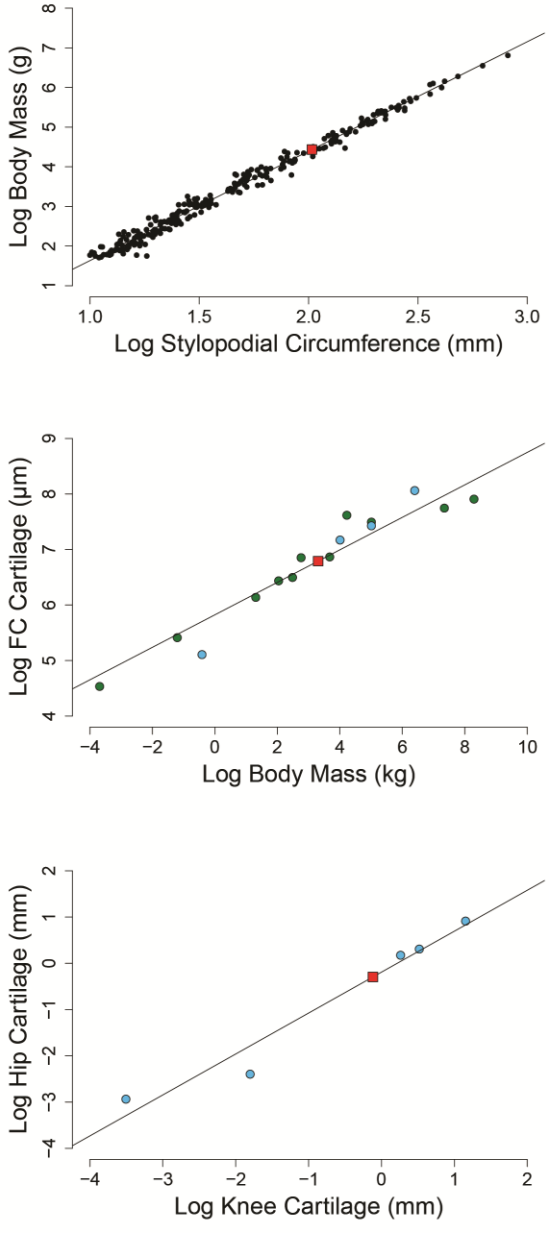

Figure 9.
Musculoskeletal models of the *D. milleri* and *M. domestica* hindlimb in Software for Interactive Musculoskeletal Modeling (SIMM) prior to adding wrap objects. The muscle paths of only 4 homologous muscles were included for illustrative purposes in each model (from left to right, 1: pubotibialis, adductor longus; 2: gracilis, gracilis; 3: flexor tibialis internus, semimembranosus; and, 4: flexor tibialis externus, semitendinosus).

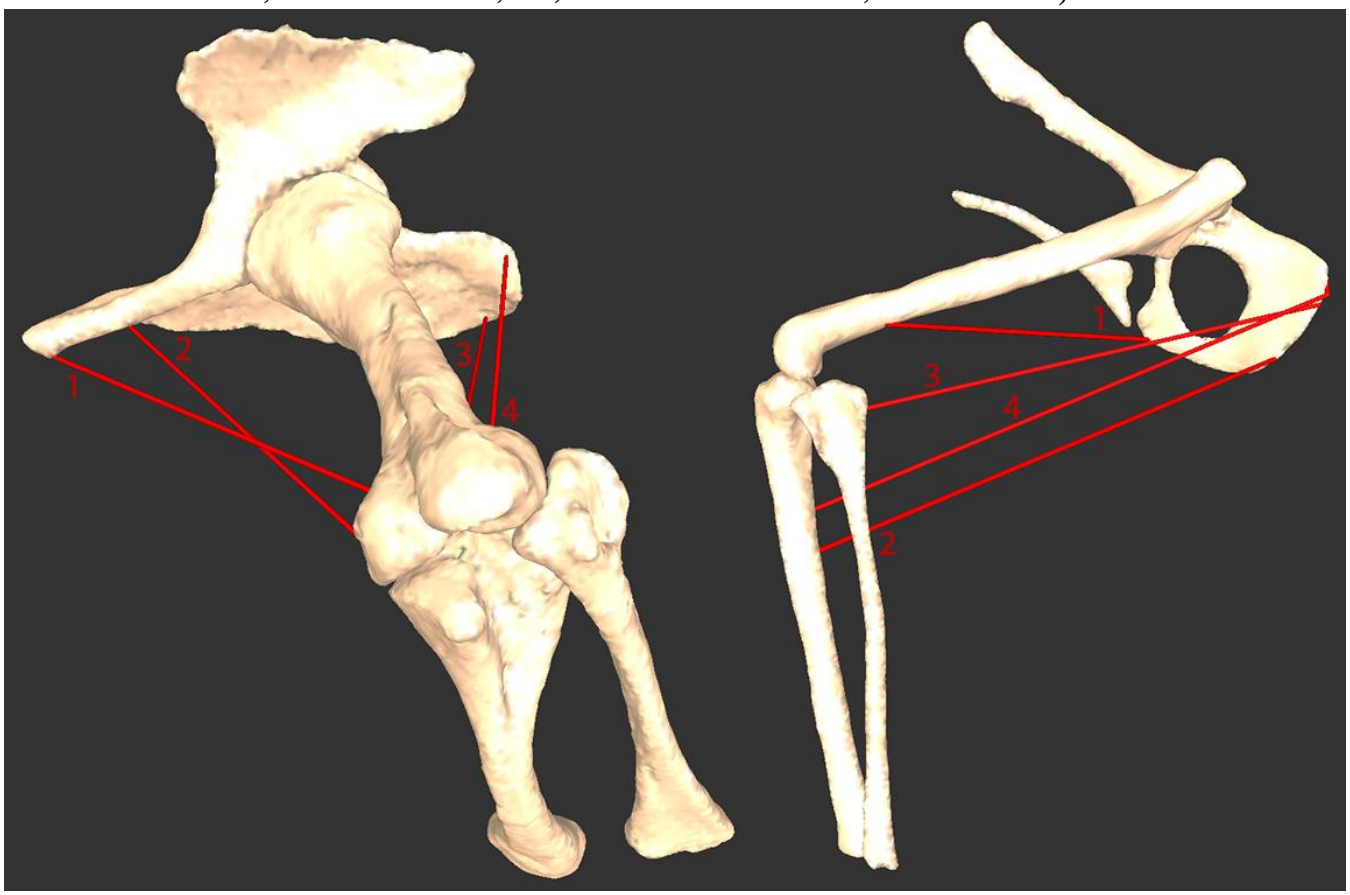

Figure 10.
The final musculoskeletal SIMM model of the *D. milleri* hindlimb, including wrap objects and via points. The hip and knee joints are oriented in a neutral pose, which was established during model construction. A total of 13 muscles were modeled that act on either the hip or knee joint. For muscle origin and insertion coordinates, see Table 6.

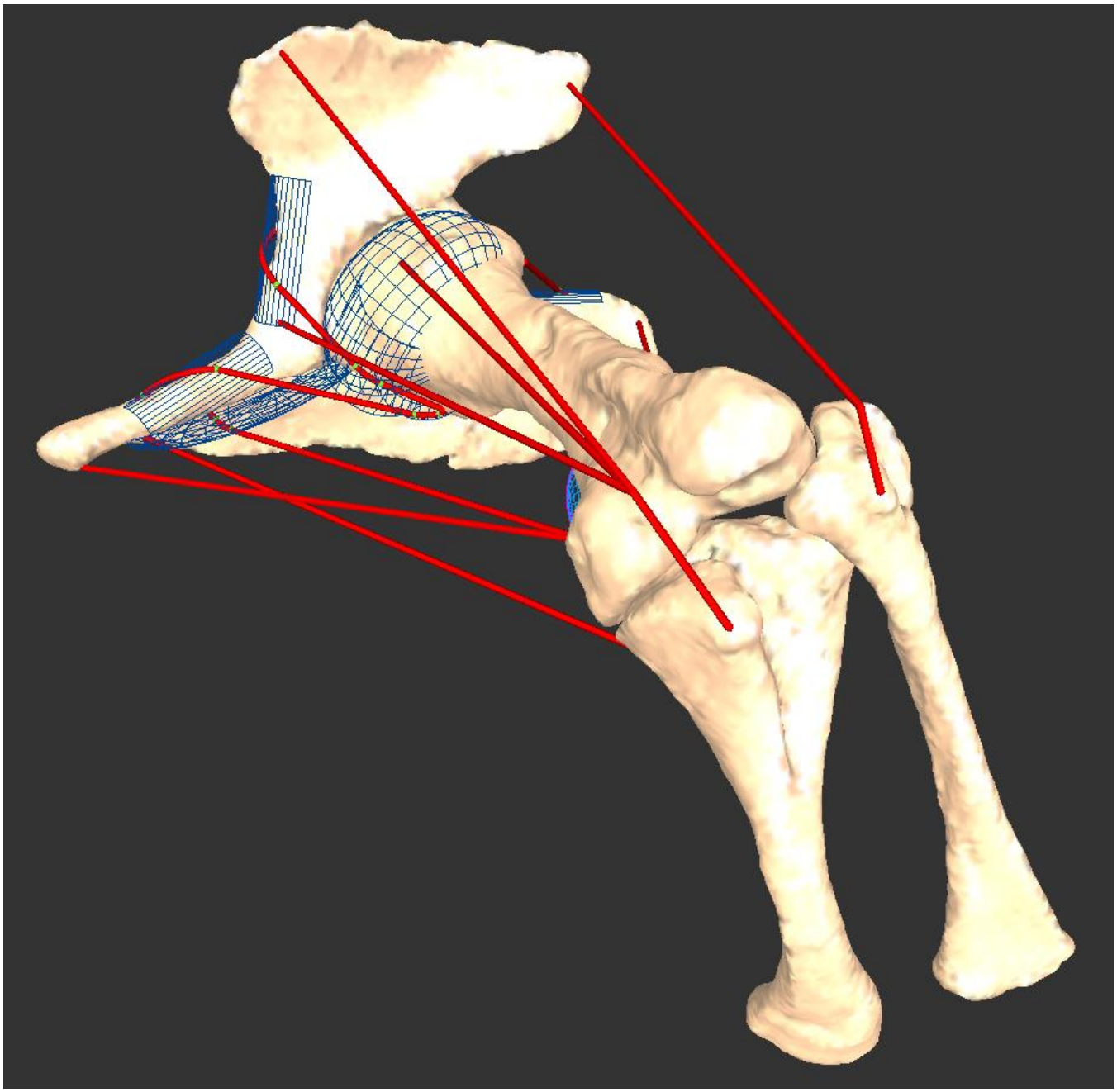

Figure 11.
The final musculoskeletal SIMM model of the *M. domestica* hindlimb, including wrap objects and via points. The hip and knee joints are oriented in the stained neutral pose, which was the position of the cadaver during the μCT scanning. A total of 23 muscles were modeled that act on either the hip or knee joint. For muscle origin and insertion coordinates, see Table 7. Left: medial; right: lateral view.

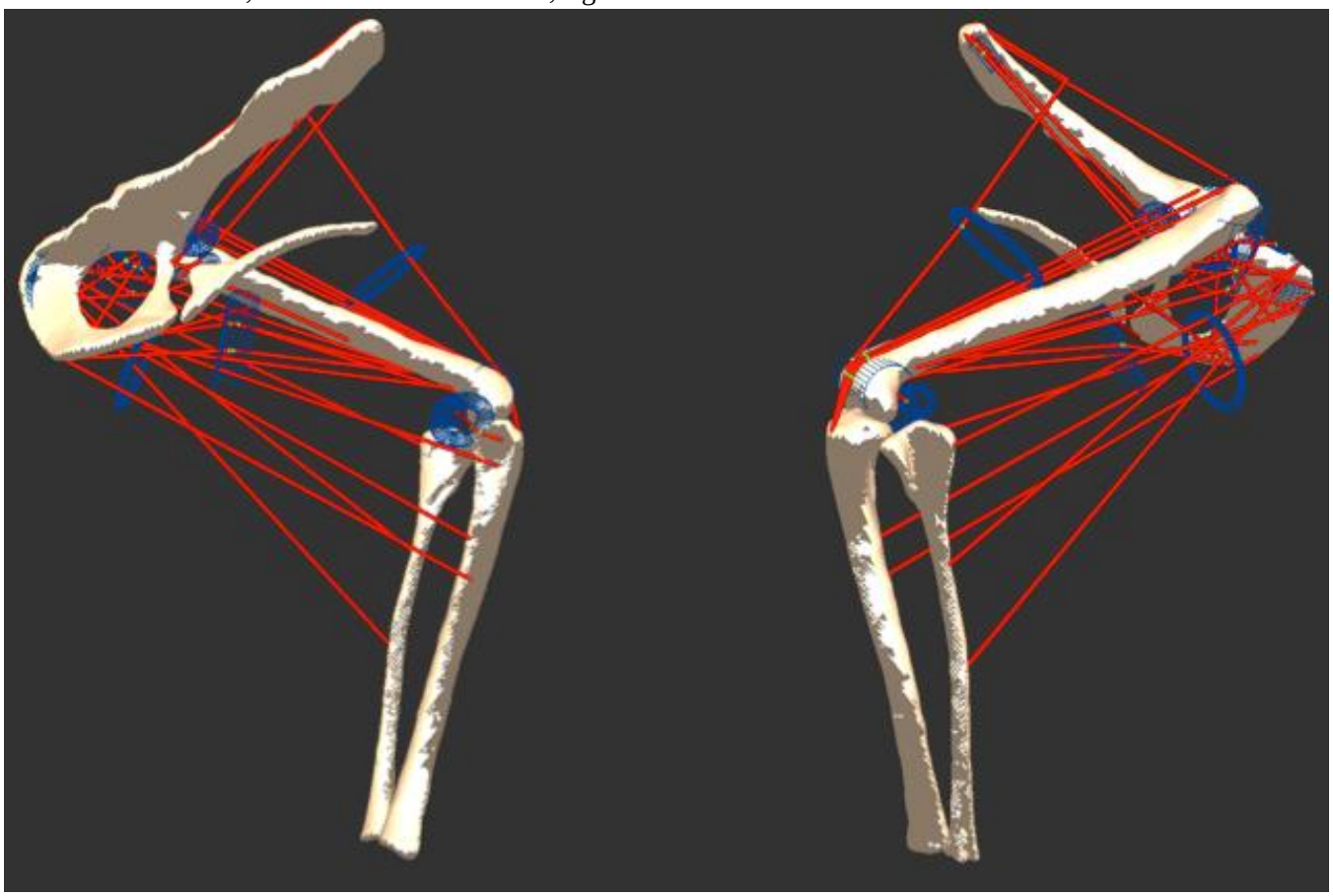

Figure 12.
Moment arm plots for each individual muscle of *D. milleri* about each rotational axis (Abduction/adduction = red, long axis rotation = green, flexion/extension = blue). Joint angle indicates range of motion (ROM) in both directions along each respective axis from the neutral pose. Moment arms are calculated for each joint angle within the muscle's ROM. Muscle abbreviations are given in Table 4.

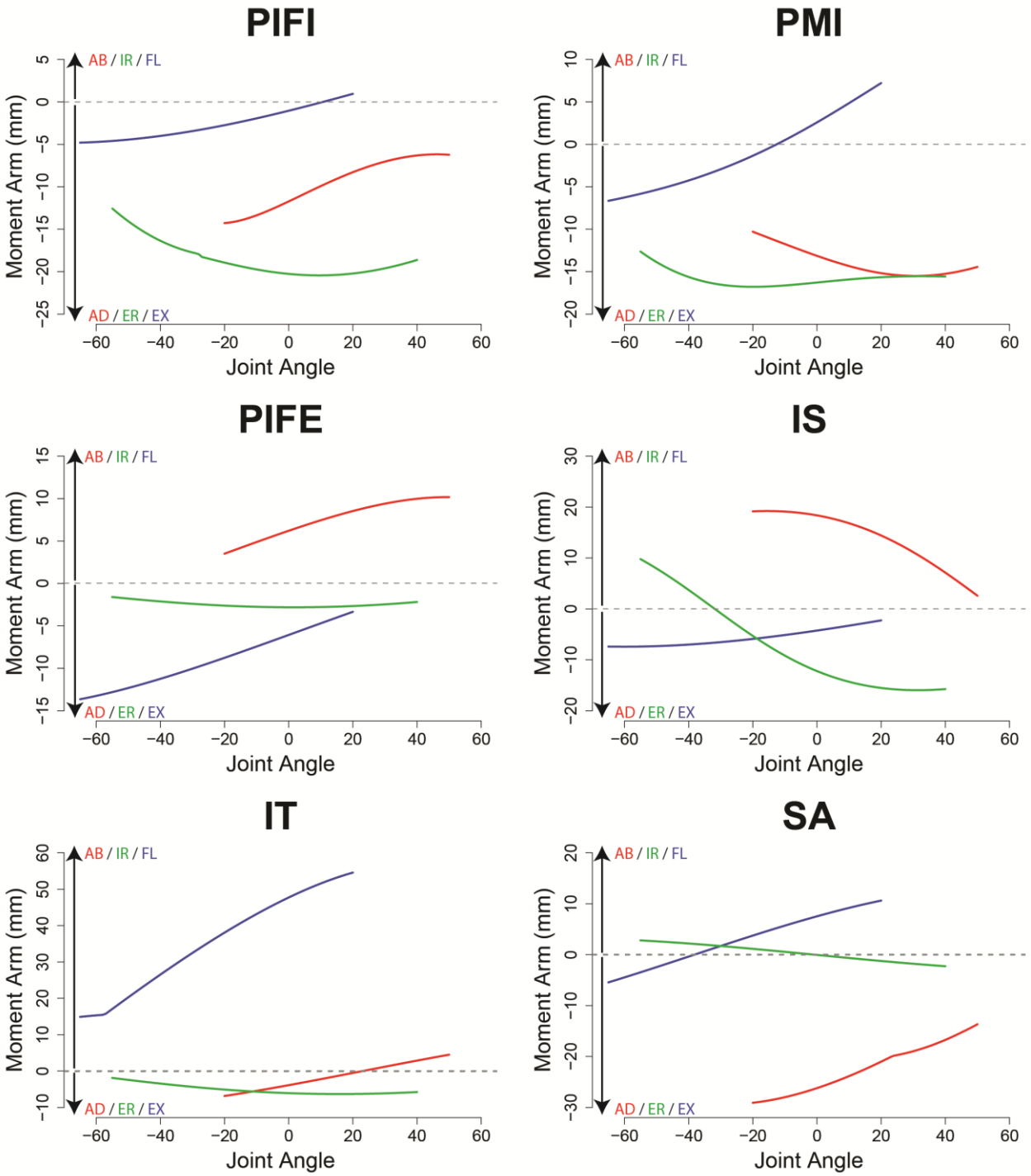

Figure 12 (Continued).

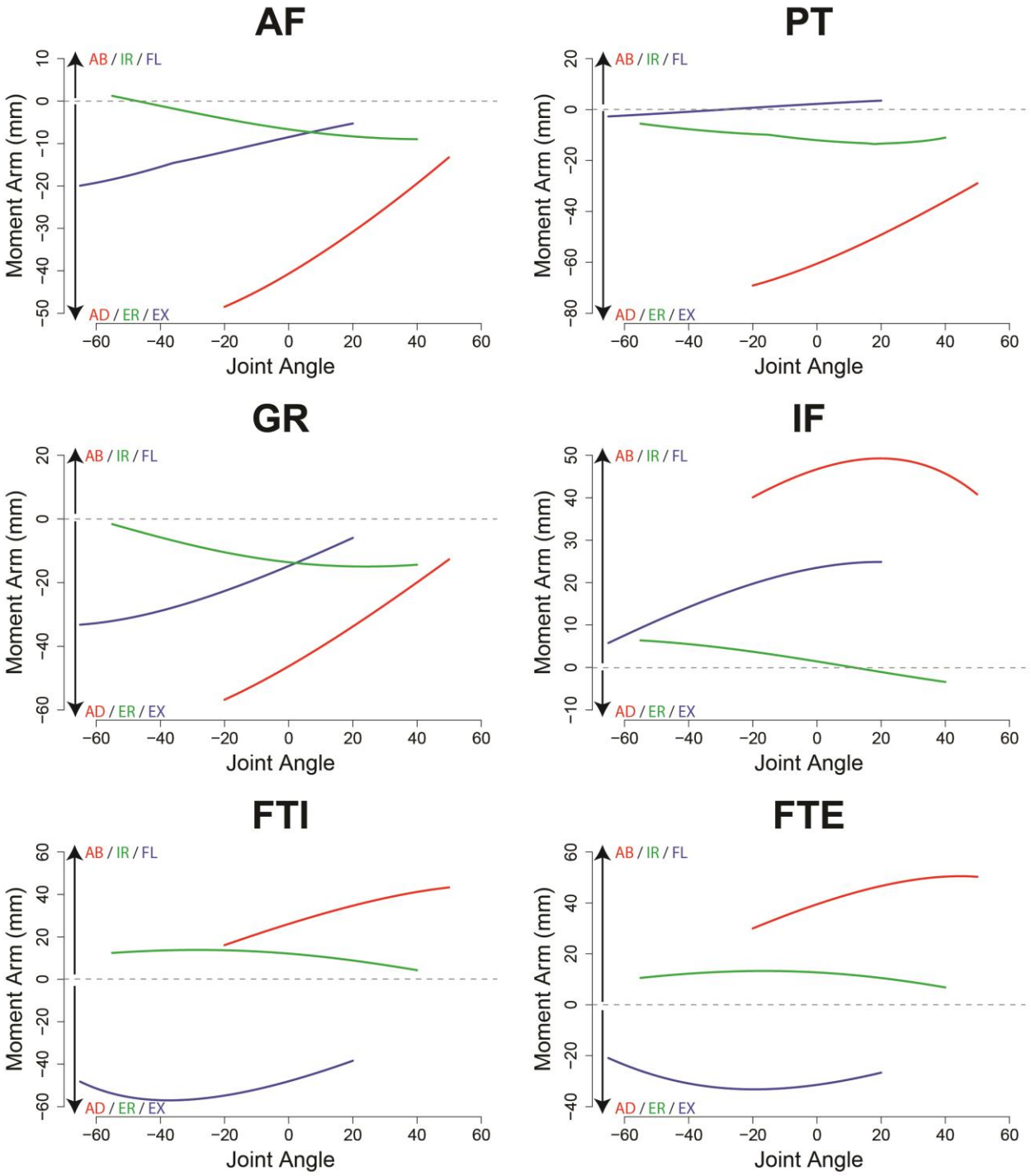

Figure 13.
Moment arm plots for each individual muscle of *M. domestica* about each rotational axis (Abduction/adduction = red, long axis rotation = green, flexion/extension = blue). Joint angle indicates range of motion (ROM) in both directions along each respective axis from the neutral pose. Moment arms are calculated for each joint angle within the muscle's ROM. Muscle abbreviations are given in Table 2.

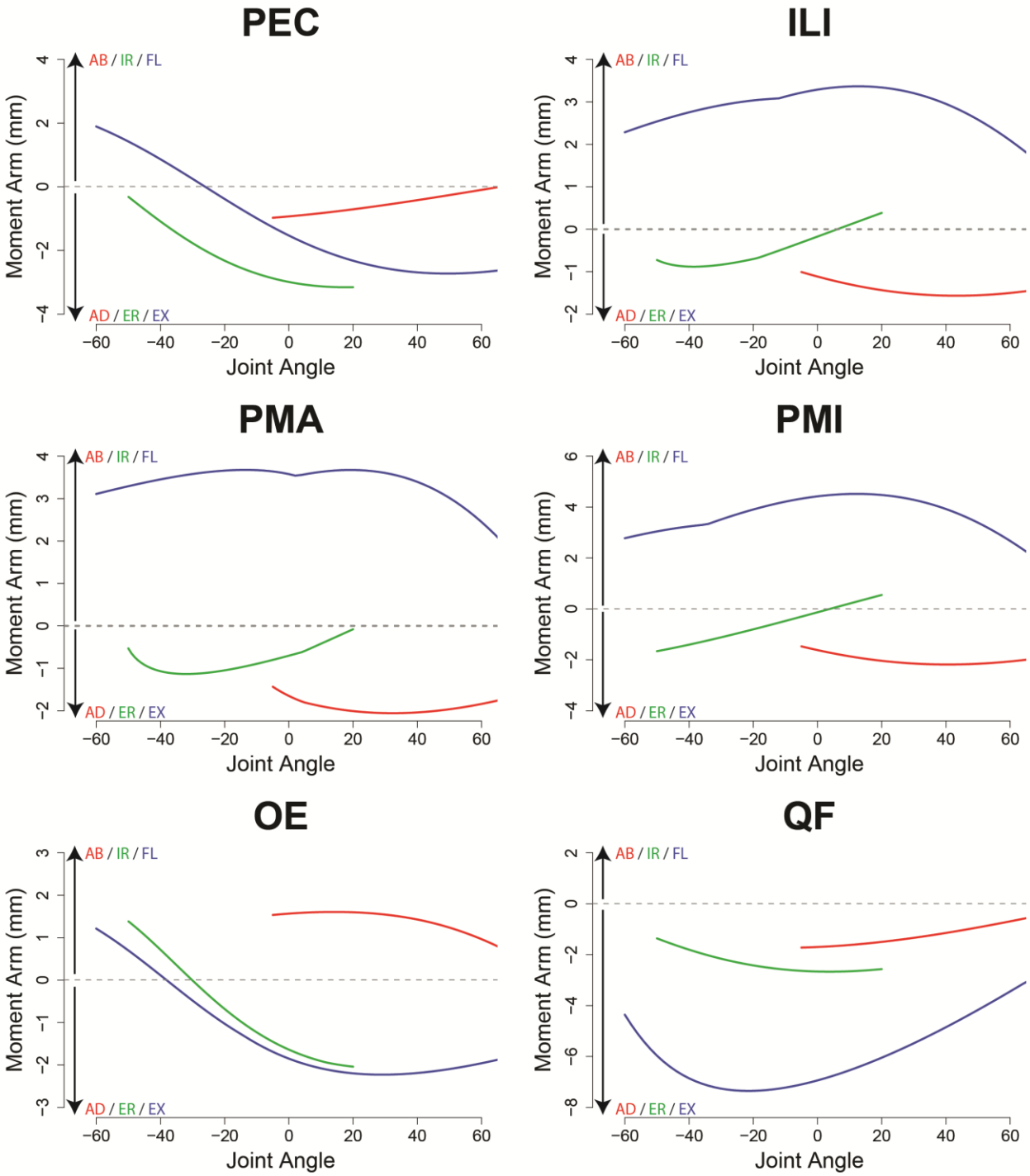

Figure 13 (Continued).

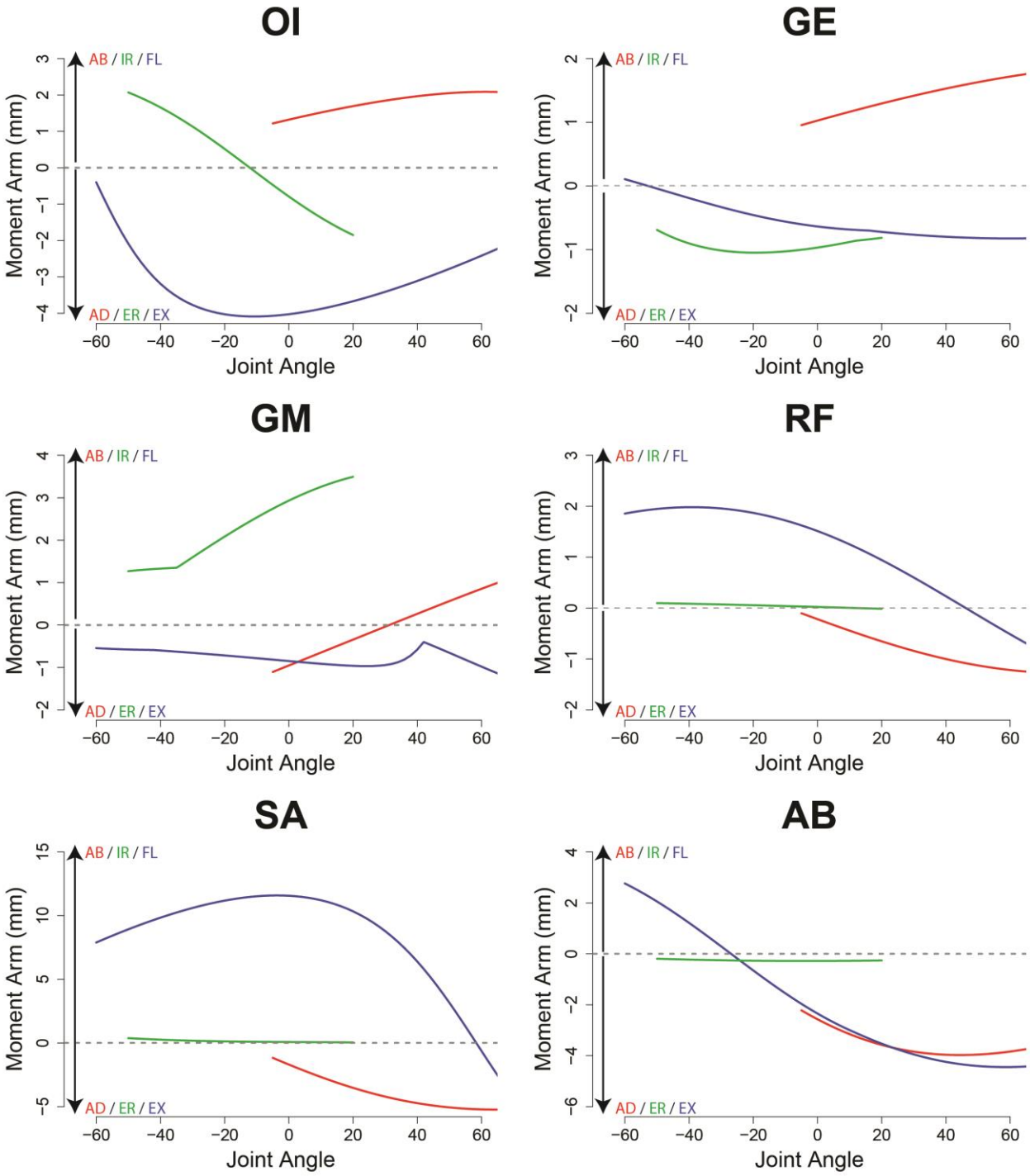

Figure 13 (Continued).

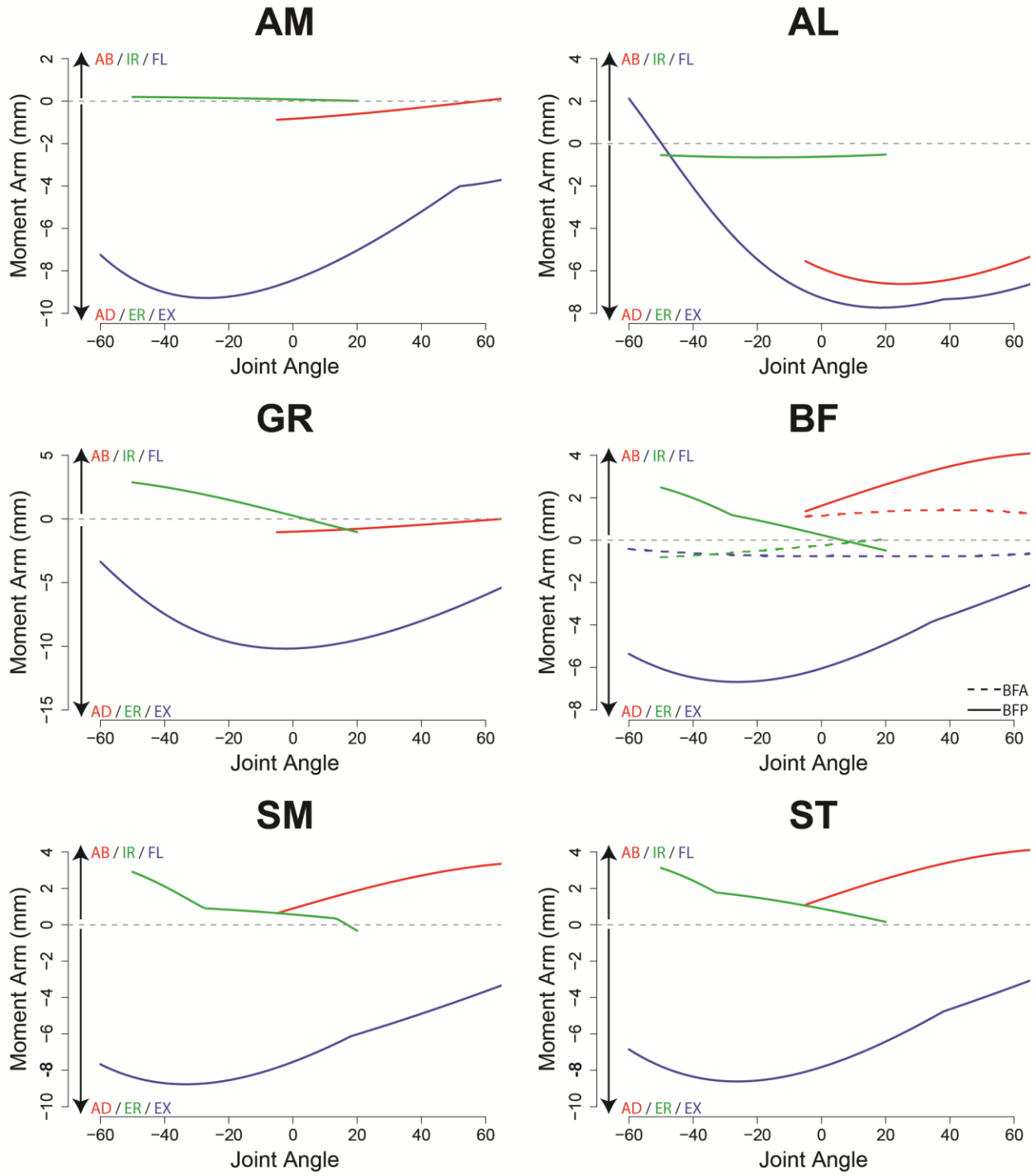

Figure 14.
Moment arm plots for homologous muscles between *D. milleri*, *M. domestica*, and *D. deserti* (where available) about each rotational axis (Abduction/adduction = red, long axis rotation = green, flexion/extension = blue). Joint angle indicates range of motion (ROM) in both directions along each respective axis from the neutral pose. Moment arms are calculated for each joint angle within the muscle's ROM.

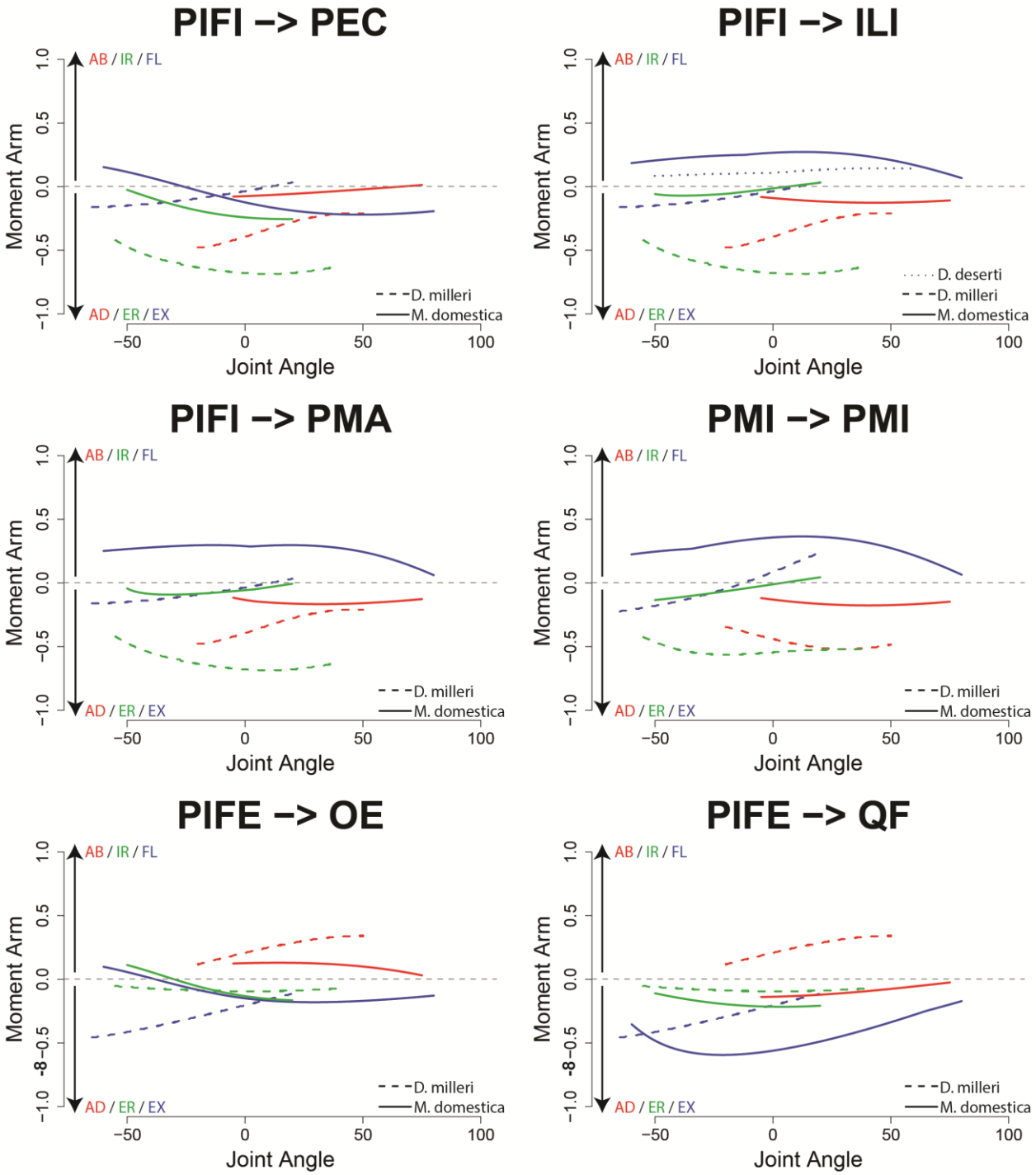

Figure 14 (Continued).

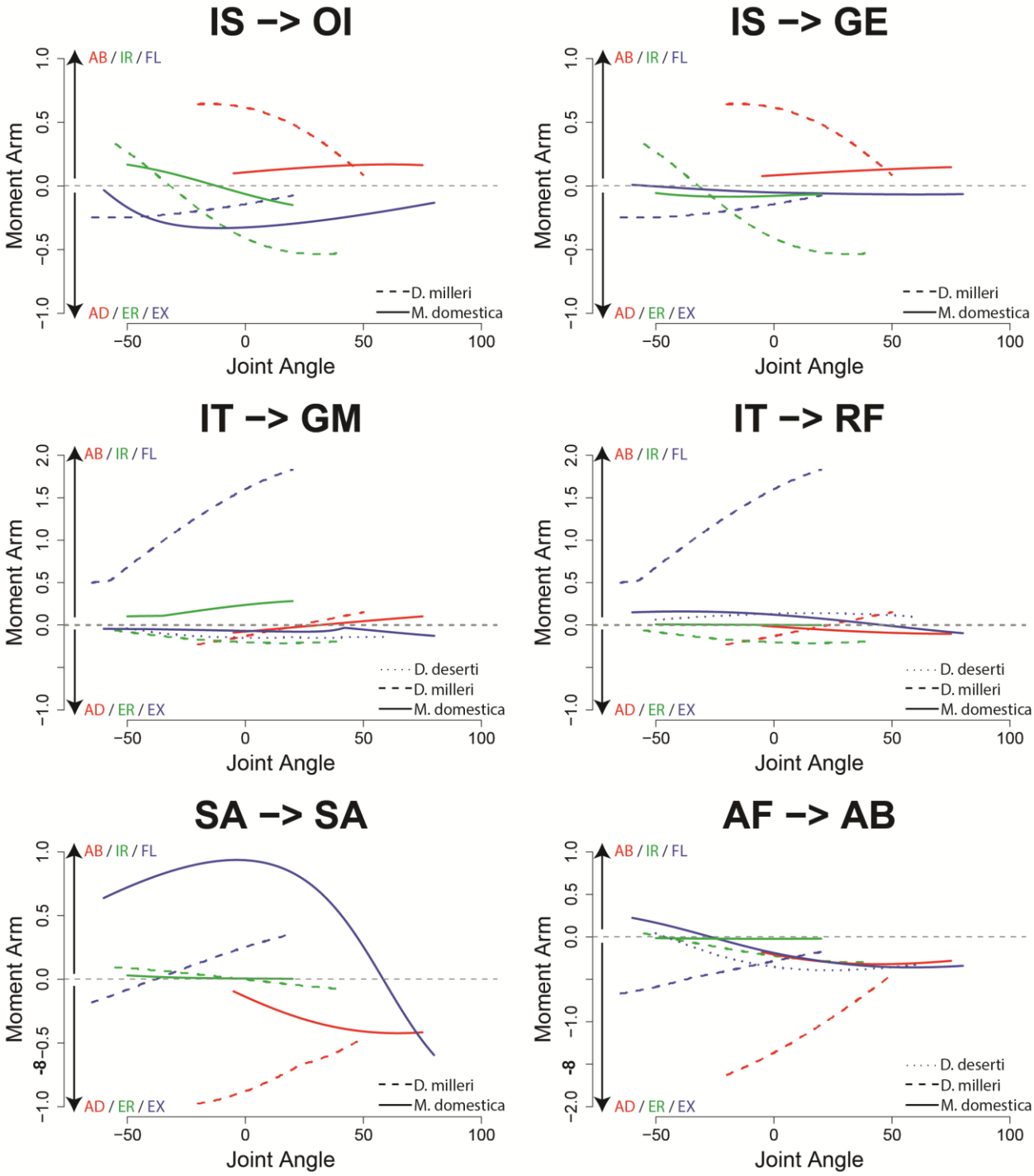

Figure 14 (Continued).

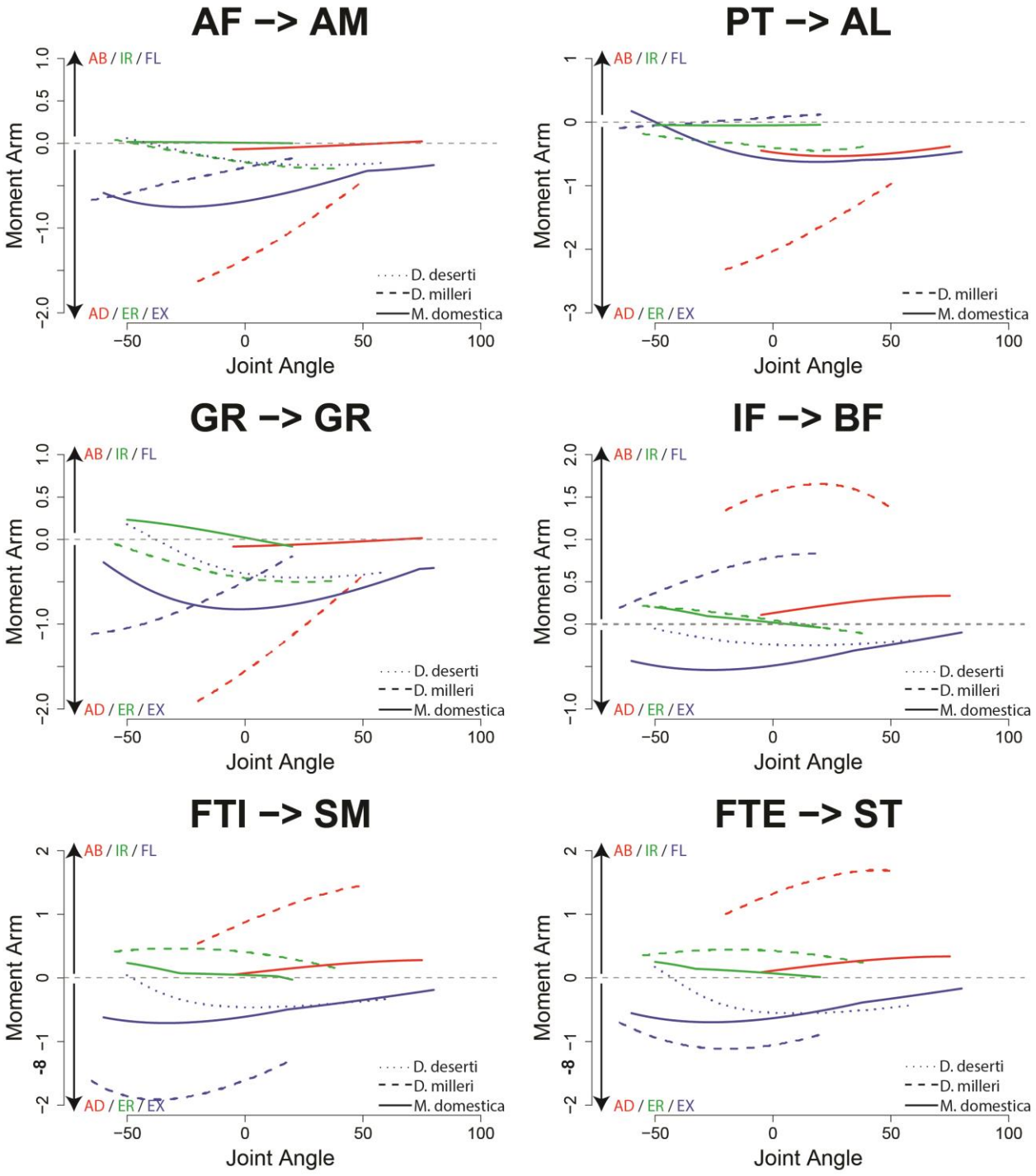

Figure 15.
Summed and normalized moment arm plots (scaled by femur length) about each rotational axis of the hip joint for *D. milleri* and *M. domestica* (Abduction/adduction = red, long axis rotation = green, flexion/extension = blue). Joint angle indicates range of motion (ROM) in both directions along each respective axis from the neutral pose.

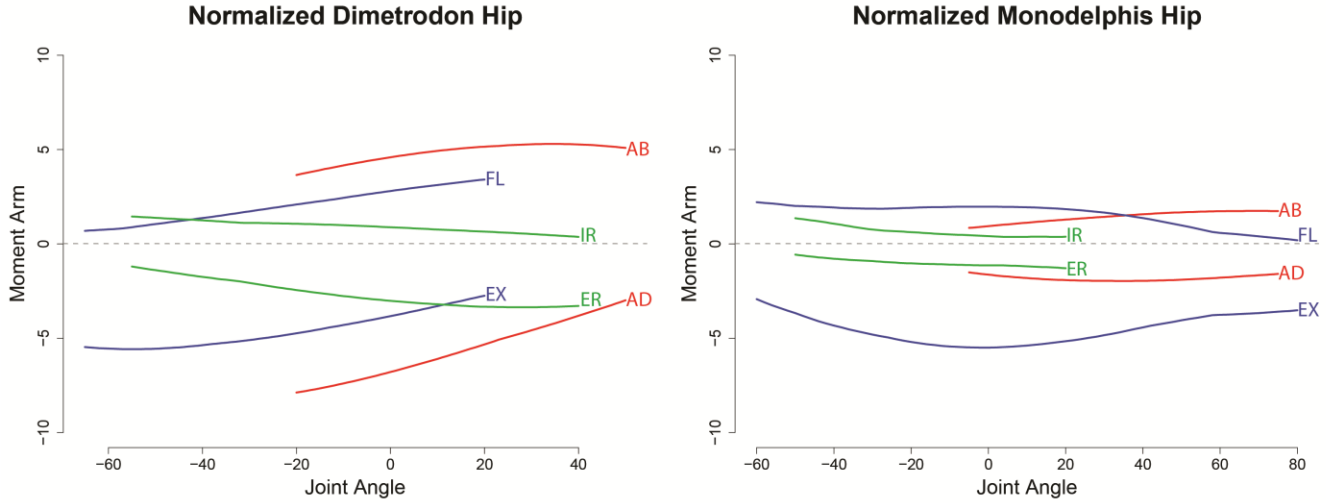

Figure 16.
Homologous muscles in *D. milleri* and *M. domestica* responsible for the reduction in moment arm magnitude along the abduction-adduction axis during this postural transition. Left (abductors) and right (adductors) include the three homologous muscles with the largest moment arm peak in *D. milleri* and their respective moment arm peak in *M. domestica*. Bottom, the orange and purple triangle underneath the bones of the hindlimb show that with the anterior extension of the ilium and the increase in length of the femur, the relative distance between the pubic tubercle and ischial tuberosity did not increase.

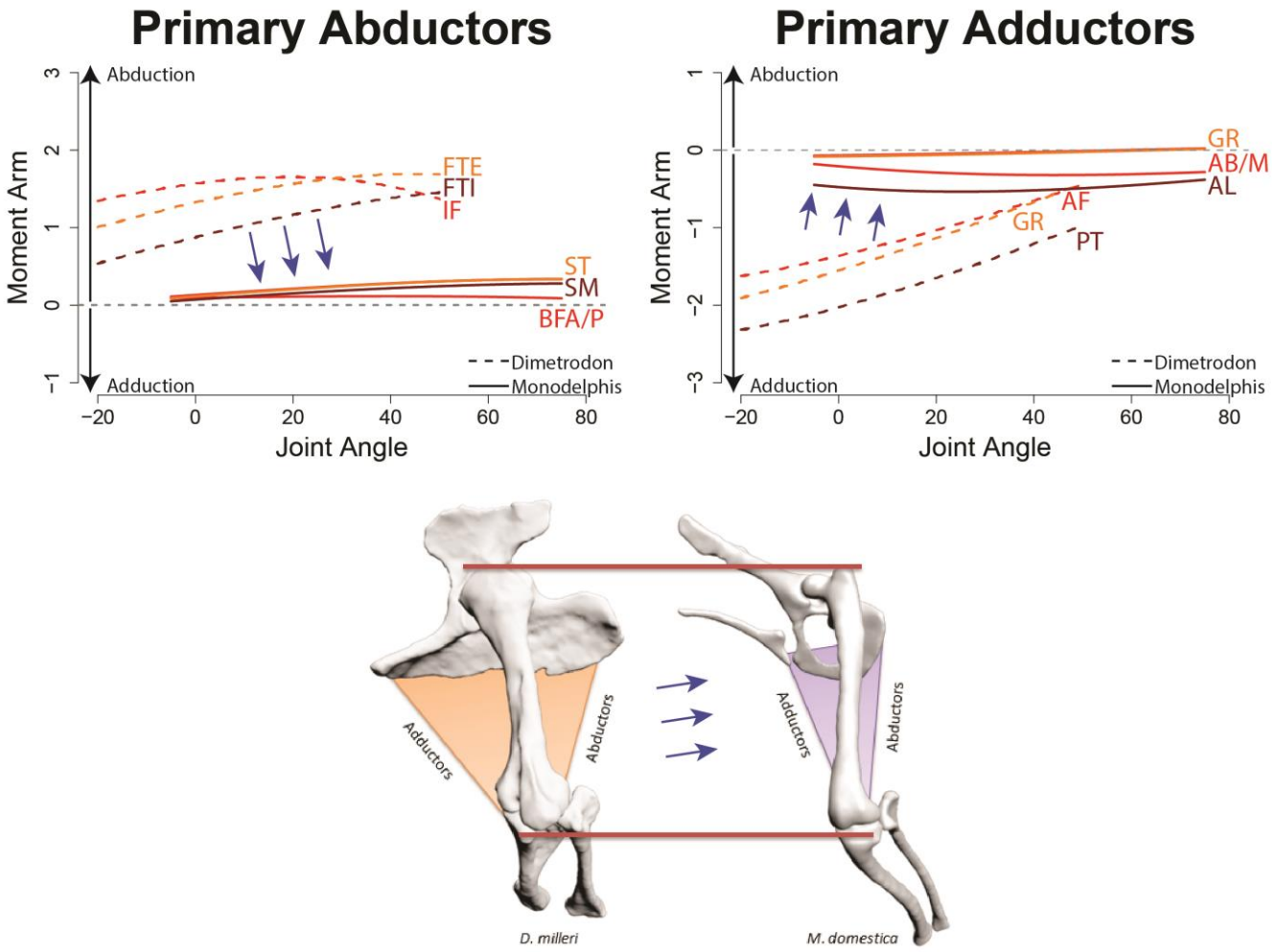

Figure 17.
Sensitivity of hindlimb pose on moment arms of 12 muscles of the hip and knee joints in *M. domestica*. Only the muscles with the highest and lowest moment arm for each functional group are pictured here: hip rotators, hip adductors, hip flexors, hip extensors, knee flexors, and knee extensors. Solid lines represent the scanned pose, dashed lines represent the 0° joint angle pose, and dotted lines represent the mid-stance pose.

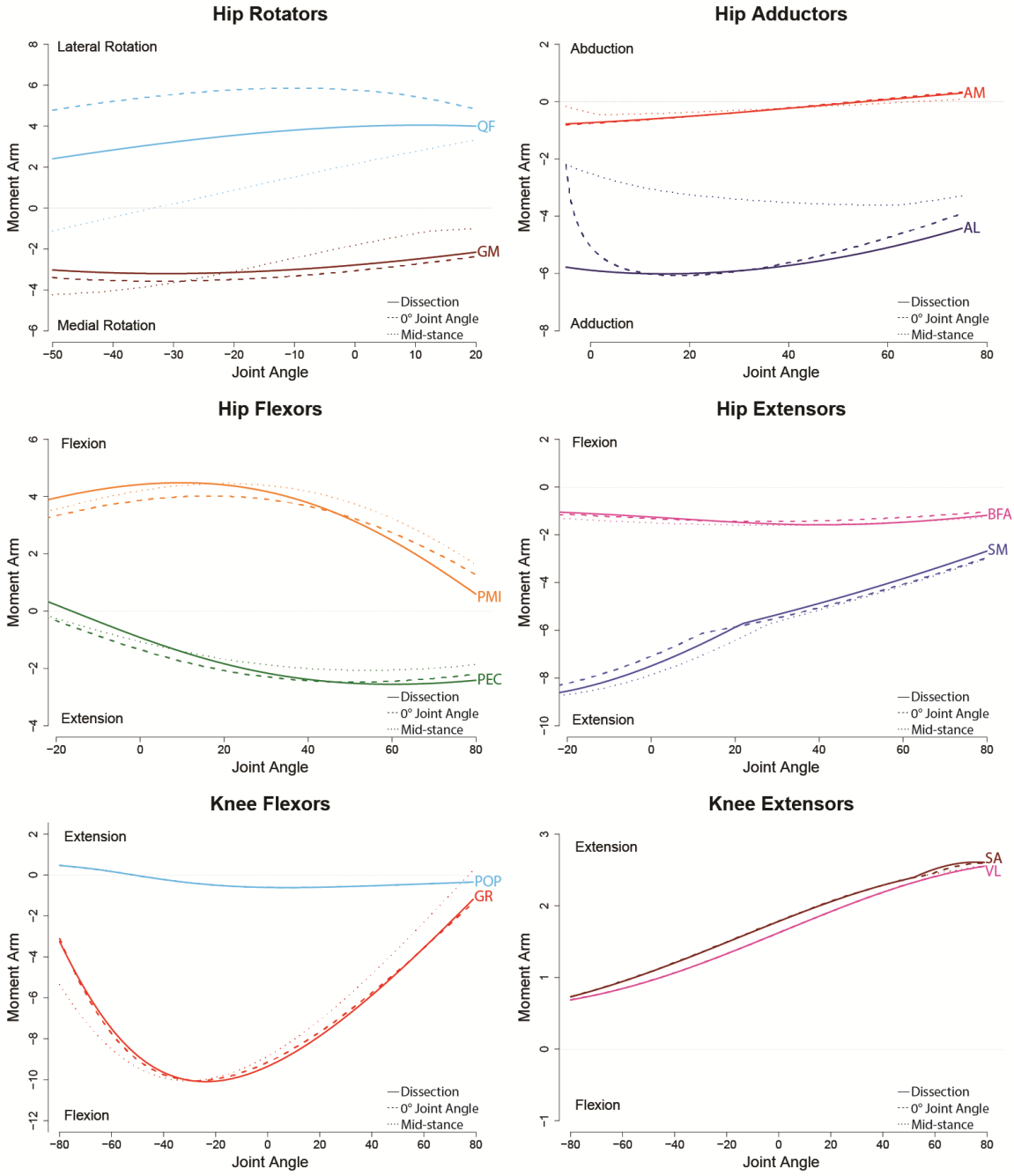

Figure 18.
Sensitivity of muscle path on moment arms of 5 muscles of the hip and knee joints with broad bony attachments in *M. domestica*: obturator externus, obturator internus, adductor longus, pectineus, and biceps femoris posterior.